Glassy dynamics in asymmetric binary mixtures of hard spheres

Edilio Lázaro-Lázaro,[1] Jorge Adrián Perera-Burgos,[2] Patrick Laermann,[3] Tatjana Sentjabrskaja,[3] Gabriel Pérez-Ángel,[4] Marco Laurati,[3,5] Stefan U. Egelhaaf,[3] Magdaleno Medina-Noyola,[1,5] Thomas Voigtmann,[6,7] Ramón Castañeda-Priego,[5,*] and Luis Fernando Elizondo-Aguilera[7,†]

[1]*Instituto de Física Manuel Sandoval Vallarta, Universidad Autónoma de San Luis Potosí, Alvaro Obregón 64, 78000 San Luis Potosí, San Luis Potosí, Mexico*

[2]*CONACYT-Unidad de Ciencias del Agua, Centro de Investigación Científica de Yucatán A.C. (CICY), Calle 8, No. 39, Mz. 29, S.M. 64, 77524 Cancún, Quintana Roo, Mexico*

[3]*Condensed Matter Physics Laboratory, Heinrich Heine University, Universitätsstraße 1, 40225 Düsseldorf, Germany*

[4]*Departamento de Física Aplicada, Cinvestav, Unidad Mérida, Apartado Postal 73 Cordemex, 97310 Mérida, Yucatán, Mexico*

[5]*Departamento de Ingeniería Física, División de Ciencias e Ingenierías, Universidad de Guanajuato, Loma del Bosque 103, 37150 León, Mexico*

[6]*Department of Physics, Heinrich Heine University, Universitätsstraße 1, 40225 Düsseldorf, Germany*

[7]*Institut für Materialphysik im Weltraum, Deutsches Zentrum für Luft-und Raumfahrt (DLR), Linder Höhe 51170, Köln, Germany*

(Received 25 July 2018; revised manuscript received 15 January 2019; published 5 April 2019)

We perform a systematic and detailed study of the glass transition in highly asymmetric binary mixtures of colloidal hard spheres, combining differential dynamic microscopy experiments, *event-driven* molecular dynamics simulations, and theoretical calculations, exploring the whole state diagram and determining the *self*-dynamics and collective dynamics of both species. Two distinct glassy states involving different dynamical arrest transitions are consistently described, namely, a double glass with the simultaneous arrest of the *self*-dynamics and collective dynamics of both species, and a single glass of large particles in which the *self*-dynamics of the small species remains ergodic. In the single-glass scenario, spatial modulations in the collective dynamics of both species occur due to the structure of the large spheres, a feature not observed in the double-glass domain. The theoretical results, obtained within the self-consistent generalized Langevin equation formalism, are in agreement with both simulations and experimental data, thus providing a stringent validation of this theoretical framework in the description of dynamical arrest in highly asymmetric mixtures. Our findings are summarized in a state diagram that classifies the various amorphous states of highly asymmetric mixtures by their dynamical arrest mechanisms.

DOI: 10.1103/PhysRevE.99.042603

I. INTRODUCTION

The binary hard-sphere (HS) mixture is one of the simplest representations of a many-body system with competing scales. Hence, it is a suitable model to investigate how the emergence of distinct timescales and length scales influences the physical behavior of a multicomponent glass-forming liquid, a question that still awaits a unified answer and with the potential to enhance the rational design of amorphous materials with high scientific and technological relevance based, for instance, on metallic alloys [1–4], polymers [5,6], colloids [7,8], and bioactive composites [9].

Colloidal suspensions of HS have played a crucial role in the study of glasses [10–13] and gels [14–16] providing neat experimental realizations of dynamically arrested states in finely controllable systems and conditions [17–24]. In the case of a *monodisperse* HS suspension, the key control parameter is the volume fraction of colloids ϕ [10,11]. Close to the glass transition (GT) point, $\phi \approx 0.58$, the relaxation of the microscopic dynamics becomes extremely sluggish despite very small changes in the structure, and the motions of individual particles are inhibited by transient *cages* formed by neighboring particles [25]. The addition of a second colloidal species with a different size drastically modifies this scenario. Even for a small size disparity ($\delta \equiv \sigma_s/\sigma_b \gtrsim 0.4$; σ_s and σ_b being the diameters of the *small* and *big* particles, respectively), this implies a significant shift of the GT point to a larger total volume fraction [26], accompanied with spatial and temporal heterogeneities, and appreciable aging effects [27,28]. For even larger degree of asymmetry (i.e., smaller δ), and depending on the composition of the mixture, different and more complex dynamical arrest transitions are observed, leading, for instance, to the formation of attractive and asymmetric glasses [29–34].

The existence of distinct glassy states in highly asymmetric binary mixtures of HS has been long known [29–40]. However, and despite several earlier studies on the dynamics of this system, presently there is no systematic and detailed investigation that explores the full parameter space and that compares experiments, simulations, and theory near the different dynamical arrest transitions observed and predicted in these mixtures. Such a comprehensive coverage, however, is

*ramoncp@fisica.ugto.mx
†luisfer.elizondo@gmail.com

crucial to obtain a deeper understanding of the glassy behavior in multicomponent systems, where distinct length scales and timescales compete in a nontrivial way, leading to a complex dynamical arrest landscape. In particular, the recent advent of differential dynamic microscopy (DDM) [31–34] renders the experimental characterization of the dynamics of both species in the large asymmetric regime possible. These advancements allow us thus to develop and test a consistent description of the GT in the binary HS model, which was missing. This provides the main motivation of this work.

We present such a description in terms of experimentally accessible quantities: the wave-vector dependent collective intermediate-scattering functions (ISF) and its single-particle counterpart, the *self*-intermediate-scattering functions (SISF). The ISF probe the overall changes in structure (on a certain wavelength) due to collective rearrangements of particles, while the SISF allow to quantify the statistics of the movements of individual particles. The latter is connected, in the low-wave-vector limit, to the mean-squared displacement (MSD) of the particles as an easily interpreted observable to quantify particle mobility. As we will show following, the different glasses that emerge in binary mixtures, called the *single* glass and the *double* glass, are best characterized by their different wave-vector dependence of the collective dynamics regarding the species-resolved ISF, and by the degree of coupling between the *self*-dynamics probed in the SISF of each species and the collective dynamics probed in the ISF. The characterization thus requires the ability to resolve both species' dynamics in experiments and simulations.

From the theoretical point of view, the well-known mode coupling theory (MCT) of the GT [41–44] laid down a strong basis for the *first-principles* description of dynamical arrest in multicomponent glass-forming liquids [33,35,36]. More recently, the self-consistent generalized Langevin equation (SCGLE) theory of dynamical arrest [45–48] has joined MCT on this endeavor [37,38]. Despite the different starting points adopted in deriving each theoretical framework, a generic asymptotic solution valid for either MCT or SCGLE can be constructed close to conditions of dynamical arrest [49]. Thus, it is not surprising to find several similarities in the results provided by both approaches when they are applied to a specific model. A prominent example is the case of a HS binary mixture with disparate sizes [35–38], where the GT scenarios of MCT and SCGLE are essentially the same and qualitatively describe the few available experimental data for colloidal HS [29–33] and the limited number of results of molecular dynamics (MD) simulations for soft-sphere mixtures [23,39,40].

To date, however, these theoretical predictions have not been rigorously and systematically validated against corresponding results of both simulations and experiments, and this provides an additional motivation for this work. We then specifically show that the SCGLE qualitatively (and often semiquantitatively) agrees with the data obtained from MD and DDM, thus providing a trustworthy fundamental tool to extrapolate the simulations and experimental results to those states or observables that are not easily accessible with both techniques, and to establish a generic picture of the physical mechanisms of glass formation in mixtures with two disparate length scales. Therefore, our work also paves the way to establish the quality of the SCGLE-based description for the technologically highly relevant situation of slowly evolving colloidal suspensions, and other more complex glassy mixtures such as polymers [5,6] and metallic alloys [1–4], using highly asymmetric binary mixtures of colloidal HS as prototypical models for multicomponent glass-forming liquids.

We combine experimental techniques based on DDM able to resolve the dynamics of the two species, extensive *event-driven* MD simulations and theoretical calculations within the SCGLE formalism, to explore the full parameter space and provide a consistent description of the different paths to amorphous solidification of these systems. We specifically show how, depending on the concentration of big and small spheres and taking into account specifically the dynamical contribution of the small and large particles, one can identify two different glassy scenarios, which are characterized by distinct dynamical features at the level of both the *self*-dynamics and collective dynamics.

We organize the data from experiments and simulations along different *paths* of state points that approach dynamical arrest by increasing the overall packing fraction in different ways. These *paths* are grouped into those that approach the *single* (S) and the *double* (D) glass, respectively. The grouping also serves to emphasize that the different ways to approach a transition (for example, by increasing the overall packing fraction at fixed composition, or by adding particles of one species) are qualitatively equivalent.

After showing that the theoretical framework provided by the SCGLE accurately describes the data for the dynamics obtained from MD simulations and DDM experiments, we employ the theory to outline the main features of each glassy state in terms of the length-scale dependence of the so-called nonergodicity parameters, leading to the development of an arrested states diagram, which qualitatively classifies all the results. Details of the simulations and experiments are provided, respectively, in Appendices A and B, whereas a brief summary of the SCGLE theory can be found in Appendix C.

II. RESULTS

We investigate two fundamentally distinct GT, referred to as *fluid* to *single* glass (F-SG) and *fluid* to *double* glass (F-DG). For this, we have studied binary mixtures of HS via *event-driven* MD simulations (see Appendix A) and colloidal HS suspensions (Appendix B) with a size ratio $\delta \approx 0.2$. The choice of this value is motivated by several reasons. First, this is a size ratio particularly interesting in terms of the physics of the mixture because the two aforementioned dynamical arrest scenarios can be investigated experimentally [31,33,35–37]. At larger values of δ, the physical mechanisms associated to the two different length scales become too similar, and hence, one of the transitions would not exist or would be more difficult to distinguish. Second, this size ratio can be realized in experiments with both particle species undergoing significant Brownian (diffusive) motion within the experimental timescale and still being resolvable. Third, a larger size disparity is not only more difficult to achieve experimentally, but also implies a significant increase in the number of small particles in the simulations and, thus, on the required computing time. Furthermore, within a reasonable range of size

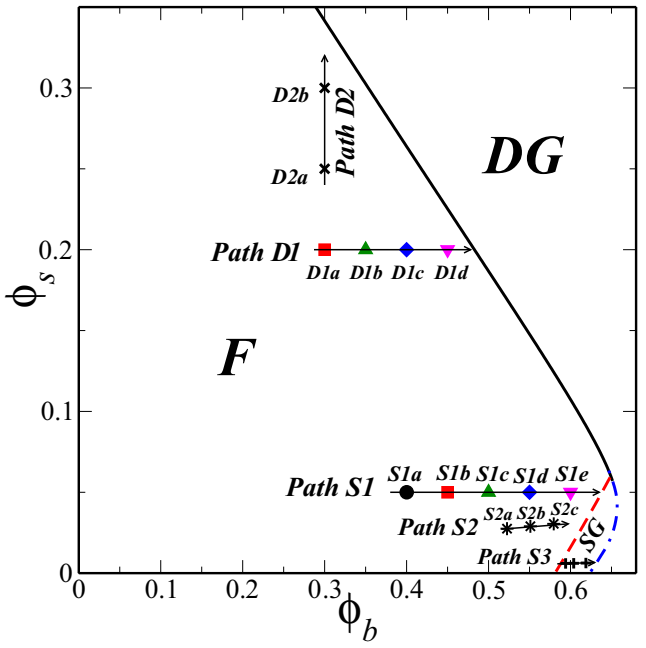

FIG. 1. State space defined by the volume fractions of big, ϕ_b, and small, ϕ_s, particles of a binary mixture of hard spheres (HS) with size ratio $\delta = 0.2$. Arrows indicate the distinct *paths* studied in this work via MD simulations (solid symbols) and DDM experiments ($+$, $*$, $\times$). All paths are also investigated with the SCGLE theory. Paths *S1,S2,S3* are used to investigate the dynamics of the transition from *fluid* to a *single* glass (F-SG), varying distinct control parameters as indicated in Table I. Paths *D1,D2* allow to study the transition from *fluid* to the *double* glass (F-DG). The lines delimiting the boundaries between regions F, SG, and DG are predictions of the SCGLE [37] for the glass transitions of a binary HS mixture ($\delta = 0.2$) using the Percus-Yevick approximation [50] combined with the Verlet-Weis correction [51] for the partial static structure factors.

ratios, the exact value of δ is not expected to play a crucial role in the determination of (metastable) *amorphous* states. This is notably different for equilibrium crystalline states, which might depend sensitively on size asymmetry. The SCGLE theory predicts that the physical scenario does not change qualitatively, for instance, when decreasing the size ratio from 0.2 to $\delta = 0.1$ (see Appendix C). Thus, we expect our results to be generic in the sense that they do not crucially depend on the size ratio, as long as δ is small enough to provide a reasonable separation of length scales. At fixed δ, the state space of a binary mixture composed of $N = N_b + N_s$ spherical particles is spanned by the two volume fractions (ϕ_b, ϕ_s), where $\phi_i \equiv \pi \rho_i \sigma_i^3/6$ $(i = b, s)$ and $\rho_i = N_i/V$. Alternatively, one could also choose the total volume fraction $\phi = \phi_b + \phi_s$ and the composition $x_s = \phi_s/\phi$ as control parameters [31–33]. For the study of the F-SG and F-DG transitions, we have considered the dynamics of the mixture at distinct state points in the plane (ϕ_b, ϕ_s), organized for clarity in different paths as shown in Fig. 1. For instance, paths *S1,S2,S3* were used to study the F-SG case, where *S1* (solid symbols) was followed using MD simulations and *S2, S3* ($*$, $+$) with DDM experiments. Similarly, we ran simulations along path *D1* (solid symbols), complemented with DDM measurements along path *D2* ($\times$)

TABLE I. List of the state points studied by means of MD simulations, DDM experiments, and SCGLE theory for the transitions from the fluid (F) state to the single glass (SG) and to the double glass (DG), respectively.

Sample	ϕ_b	ϕ_s	SCGLE	MD	Expt.	Transition
S1a	0.40	0.05	✓	✓	×	F-SG
S1b	0.45	0.05	✓	✓	×	F-SG
S1c	0.50	0.05	✓	✓	×	F-SG
S1d	0.55	0.05	✓	✓	×	F-SG
S1e	0.60	0.05	✓	✓	×	F-SG
S2a	0.5225	0.0275	✓	×	✓	F-SG
S2b	0.551	0.029	✓	×	✓	F-*SG*
S2c	0.5795	0.0305	✓	×	✓	F-SG
S3a	0.594	0.006	✓	×	✓	F-SG
S3b	0.6039	0.0061	✓	×	✓	F-*SG*
S3c	0.6138	0.0062	✓	×	✓	F-SG
D1a	0.30	0.20	✓	✓	×	F-DG
D1b	0.35	0.20	✓	✓	×	F-*DG*
D1c	0.40	0.20	✓	✓	×	F-DG
D1d	0.45	0.20	✓	✓	×	F-DG
D2a	0.30	0.25	✓	×	✓	F-DG
D2b	0.30	0.30	✓	×	✓	F-DG

to test the F-DG transition. In all cases, we investigate the dynamics at the same state points also using the SCGLE theory. To facilitate the discussion, all the state points explored are summarized in Table I.

Let us mention in advance that the two lines delimiting the boundaries of the F region in Fig. 1, and the line separating region SG from DG, correspond to theoretical predictions of the SCGLE for the GT in a HS binary mixture, with $\delta = 0.2$, using the Percus-Yevick approximation [50] combined with the Verlet-Weis correction [51] for the partial structure factors. After presenting the main results from MD and DDM, we provide a detailed discussion concerning the determination of these transition lines and other features predicted by the SCGLE (Sec. II D). The main details of the theory are provided in Appendix C and can also be found in Ref. [37].

A. Dynamics of the F-SG transition

To describe the dynamics of the mixture towards the F-SG transition, let us start with path *S1*. As shown in Table I, this path considers a fixed $\phi_s = 0.05$ while increasing ϕ_b, and was investigated via SCGLE and MD simulations, thus allowing to resolve both the self-dynamics and collective dynamics of the two species.

Figures 2(a) and 2(b) display a comparison of the SCGLE predictions and MD results, respectively, for the behavior of the SISF, $F_i^S(q,t) \equiv \langle \exp[i\mathbf{q} \cdot \Delta\mathbf{R}^{(i)}(t)] \rangle$, evaluated at $q^* = 7.18$, where $\Delta\mathbf{R}^{(i)}(t)$ denotes the displacement of *any* of the N_i particles of species i $(= b, s)$ over a time t, $\mathbf{q}$ is the scattering vector, and the reduced wave number $q^* \equiv q\sigma_b$ is used. To allow for a one-to-one comparison between the SCGLE results and the MD simulations, we have used the *molecular* version of the SCGLE theory [52] (see also Sec. 2 of Appendix A).

As shown in these figures, the SISF of the small particles (open symbols) decay much faster than those of the large

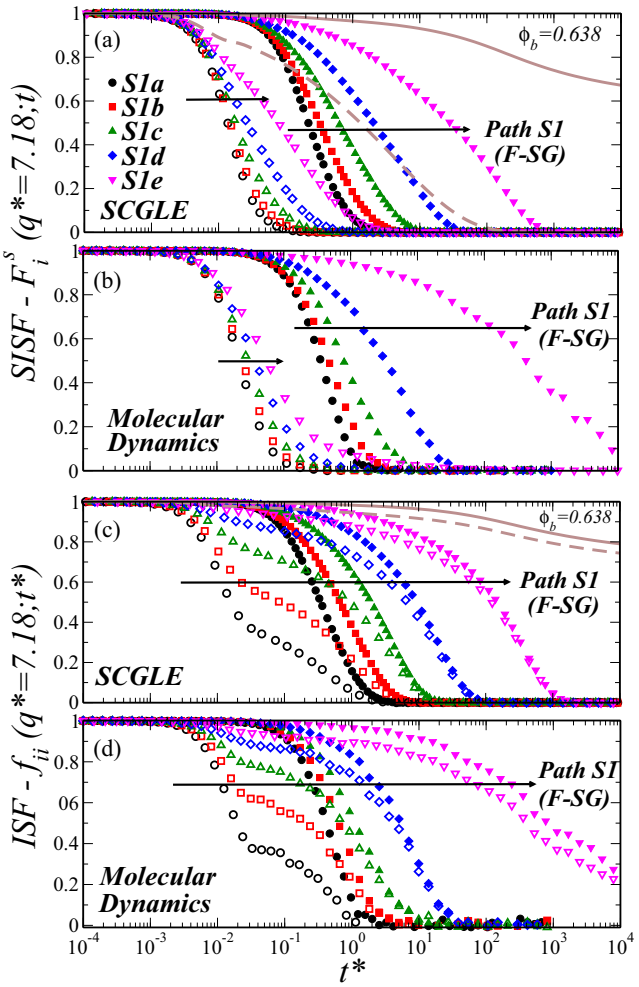

FIG. 2. Self- and collective-intermediate-scattering functions (SISF and ISF) of the large and small particles, calculated along the state points of path *S1* (as indicated), at fixed reduced wave number $q^* \equiv q\sigma_b = 7.18$, and as a function of the reduced time $t^* \equiv t/t_b^0$, where $t_b^0 = \sigma_b\sqrt{M_b/k_BT}$, M_b is the mass of any of the large particles, k_B the Boltzmann constant, and T the absolute temperature (see Ref. [52] and Appendix A). (a) Results of the SCGLE theory for the SISF $F_b^S(q^* = 7.18, t^*)$ (solid symbols) and $F_s^S(q^* = 7.18; t^*)$ (open symbols), including the solid and dashed curves for, respectively, the big and small particles, at the critical value $\phi_b^{(g)} = 0.638$. (b) Corresponding results obtained with event-driven MD simulations. (c), (d) Corresponding results for the ISF $f_{bb}(q^* = 7.18, t)$ (solid symbols) and $f_{ss}(q^* = 7.18, t)$ (open symbols).

ones (solid symbols) at all the state points of path *S1*. Upon increasing ϕ_b, a general slowing down is observed in both F_s^S and F_b^S, but the slowdown is much more pronounced for the large particles. This scenario is essentially the same in both theory and simulations, except for small differences in timescales. The MD results show a slightly faster decay of F_b^S for low ϕ_b (*S1a–S1d*) and a slower decay for large ϕ_b (*S1e*). In addition, in the simulations F_s^S develops a final stretched relaxation pattern that is reminiscent of that seen in the dynamics of tracers moving in crowded environments [33], for instance, diffusion in heterogeneous porous media [53].

The SISF of the small species always decays to zero, in contrast with that of the large spheres, which becomes much slower and eventually does not decay within the observation time window of the MD simulations. Furthermore, the theory predicts that F_b^S eventually develops a two-step relaxation, characteristic of the GT of a HS system, and occurring at the critical volume fraction $\phi_b^{(g)} = 0.638$ [solid line in Fig. 2(a)]. This state point, however, has no counterpart in the simulations because aging effects, which are observed even at *S1e*, become too severe. Also, the MD simulations at *S1e* show a static structure of the large particles that is very different from the other state points along path *S1*, although it is compatible with that of a highly amorphous solid (see Sec. 3 of Appendix A). Thus, at the level of self-dynamics, only the large species shows a signature of arrest.

We now turn to the collective dynamics and consider the *normalized* ISF, $f_{ii}(q,t) \equiv F_{ii}(q,t)/S_{ii}(q)$, with $F_{ii}(q,t) = \langle\sum_{j,k}^{N} \exp\{i\mathbf{q}\cdot[\mathbf{r}_j^{(i)}(t) - \mathbf{r}_k^{(i)}(0)]\}\rangle/N$, where $\mathbf{r}_j^{(i)}(t)$ describes the position of the jth particle of species i at time t, and $S_{ii}(q)$ denotes the corresponding partial static structure factor [i.e., $S_{ii}(q) = F_{ii}(q, t = 0)$]. Figures 2(c) and 2(d) display the predictions of the SCGLE compared to MD data for $q^* = 7.18$, which both provide essentially the same scenario. One notices first that the behavior of f_{bb} is essentially the same as that of F_b^S, in contrast with f_{ss} which qualitatively differs from F_s^S. At the state point *S1a*, for instance, the relaxation patterns of the SISF and ISF of the small species are clearly distinct (open circles), where the latter exhibits a two-step relaxation pattern not observed in the former. Upon increasing ϕ_b, f_{ss} gradually evolves and eventually follows the same trend as f_{bb}, not only at long delay times but for almost all times. This feature is not observed in the self-dynamics. Thus, approaching the F-SG transition the *normalized* collective ISFs of both species become slower and coupled at wave number $q^* = 7.18$. These features are qualitatively the same in both SCGLE and MD results, although in the MD results one observes again slightly different relaxation times.

Let us now consider path *S2*, along which $x_s = 0.05$ is fixed (rather than fixing ϕ_s) and ϕ increases toward the F-SG transition. As mentioned before, this path was investigated by means of DDM experiments yielding the ISF of the two species. The results are shown in Fig. 3. Despite the limited time window of the experiments (lower panel), one notices that the measured ISF display similar behavior as that found along path *S1*, where with increasing concentration both correlation functions become slower and f_{ss} starts to follow, in particular at long times f_{bb}. The qualitative similarity between the results of paths *S1* and *S2* suggests that the overall dynamical scenario does not depend on the specific route along which the transition is approached.

We have additionally analyzed the q^* dependence of $f_{ii}(q^*, t^*)$ for the more concentrated samples along paths *S1* and *S2*, i.e., the points *S1e* and *S2c*. Results for both state points show good qualitative agreement between theory, simulations, and experiments, as shown in Figs. 4 and 5, respectively. Both f_{bb} and f_{ss} display an initial acceleration of the decay with increasing q^*, a slowing down for $q^* = 7$, and a second acceleration for larger q^* at the state point *S1e*. As we will discuss later in Sec. II D, these effects can be attributed to the modulation of the structure factor of large particles.

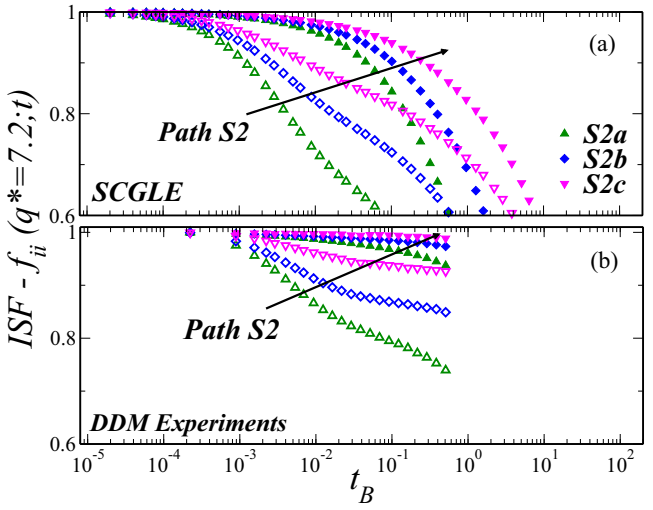

FIG. 3. Collective ISF of the large $f_{bb}(q^*, t)$ (solid symbols) and small $f_{ss}(q^*, t)$ (open symbols) particles along path *S2* (as indicated), at fixed $q^* = 7.20$ as a function of the scaled time $t_B \equiv t/\tau_B$, where $\tau_B = \sigma_b^2/D_b^0$. The top panel displays predictions of the SCGLE and the bottom panel DDM measurements. To scale experimental data, we used $\tau_B = 150s$ (see Appendix B).

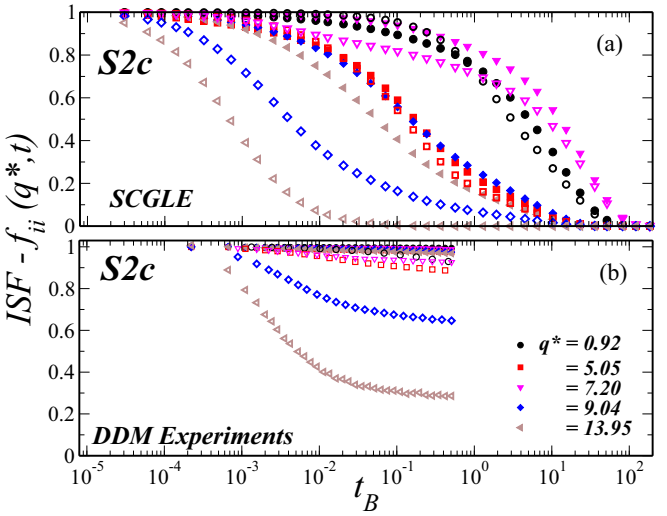

FIG. 5. Collective ISF for the large $f_{bb}(q^*, t^*)$ (solid symbols) and small $f_{ss}(q^*, t^*)$ (open symbols) particles, at the state point *S2c*, for different wave numbers q^* (as indicated) as a function of the scaled time t_B. The top panel displays predictions of the SCGLE theory and the bottom panel DDM measurements.

Additionally, for $q^* > 7$, f_{ss} develops distinct relaxation patterns to those observed in f_{bb}; a faster initial decay followed by an intermediate inflection point, whose height *oscillates* with increasing q^*. This reflects the increasingly smaller fraction of small particles that are temporarily trapped at increasingly shorter length scales (larger q^* values). These features are also observed in the experimental results at *S2c* displayed in Fig. 5, although with some minor quantitative differences with respect to the theory, thus suggesting a void

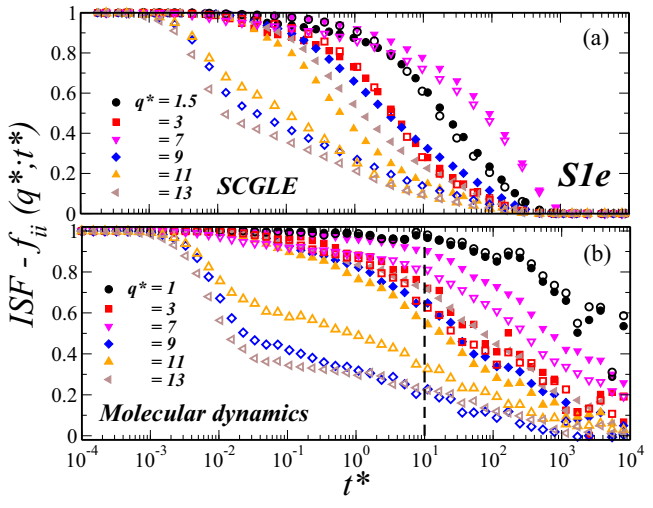

FIG. 4. Collective ISF of the large $f_{bb}(q^*, t^*)$ (solid symbols) and small $f_{ss}(q^*, t^*)$ (open symbols) particles, at the state point *S1e*, for different wave numbers q^* (as indicated) as a function of the reduced time t^*, obtained from the SCGLE theory (upper panel) and MD (lower panel). The vertical dashed line in the lower panel indicates $t^* = 10$, at which the values $f_{ii}(q^*, t)$ have been extracted for the comparison in Fig. 15(a).

structure slightly different in the theoretical and experimental samples or hydrodynamic interactions playing a significant role.

One notices that for samples *S1e* and *S2c*, experiments and simulations are consistent with the theoretical predictions. The data display essentially the same behavior and the structural relaxation times are roughly equal for $q^* \lesssim 7$. The two samples correspond, however, to overall packing fractions $\phi = 0.65$ and 0.60, respectively. Hence, the results support the theoretical prediction that, toward the F-SG transition, the total volume fraction to reach the GT in the binary mixture increases upon the addition of small particles [36,37].

To further investigate the influence of both ϕ_s and ϕ_b on the dynamics of the small particles close to the F-SG scenario, we also consider path *S3*, which corresponds to experimental data previously reported for $f_{ss}(q^*, t)$, at $\phi \approx 0.61$ and $x_s = 0.01$ (i.e., $\phi_s \approx 0.006$, see Table I) [33]. The results displayed in Fig. 6 show that, in comparison to paths *S1* and *S2* (where $\phi_s = 0.05$ and $\phi_s \approx 0.03$, respectively), the height of the plateaus in f_{ss} is generally lower at comparable q^* values. This implies that due to crowding, i.e., increasing ϕ_s, localization involves a larger fraction of small particles down to smaller length scales. Again, experiment and SCGLE are in good overall agreement. However, obvious differences arise at $q^* \approx 7$. This value corresponds to the length scale set by the nearest-neighbor cages of big particles, and it is associated to a strong peak in the static structure factor of the large species. The differences may represent the deviations of the idealized binary HS mixture assumed in the theoretical calculations from the experimental model system. For example, in the experimental samples, both species are polydisperse to avoid crystallization. Thus, one expects that density fluctuations around the value $q^* \approx 7$ will be noticeably affected by the degree of polydispersity in the large particles; this is not accounted for in the theory. For the strictly binary model system, one

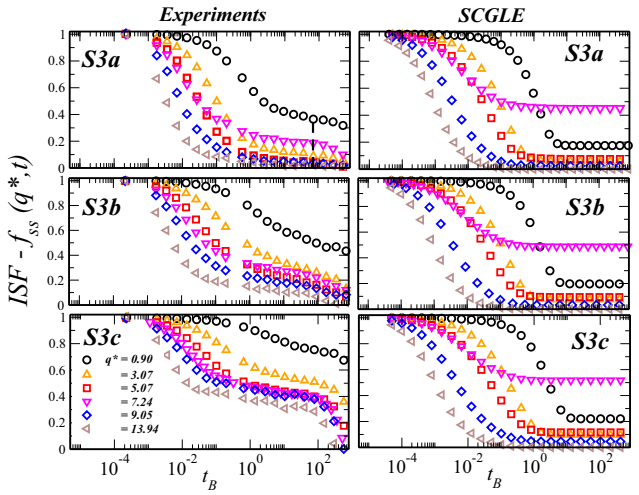

FIG. 6. Collective ISF of the small particles $f_{ss}(q^*, t)$ along path *S3* for different values of q^* (as indicated) as a function of the scaled time t_B. Left column: experimental results reported in Ref. [33]. Right column: SCGLE predictions for the same state points. The vertical dashed line in the upper left panel indicates the time $t_B = 66.7$ (i.e., $t = 10^4$ s), at which the values $f_{ss}(q^*, t_B = 66.7)$ were extracted for the comparison shown further below in Fig. 15(c).

observes important variations in both the static structure factor and the $f_{bb}(q, t)$ around $q^* = 7$ that are strongly smeared out due to polydispersity. Hence, a comparison of plateau values at this length scale overemphasizes the differences in the q-dependent structure functions.

We finally consider the behavior of the mean-squared displacements (MSD) along path *S1*. Figure 7 reports a comparison of the results obtained from MD (symbols) and SCGLE (lines). The features of the self-dynamics toward the F-SG transition previously illustrated in terms of the SISF [Figs. 2(a) and 2(b)] are also manifested in the corresponding MSDs $W_i^*(t; \phi_b, \phi_s) \equiv \langle(\Delta r_i(t))^2\rangle/6\sigma_b^2$ $(i = s, b)$.

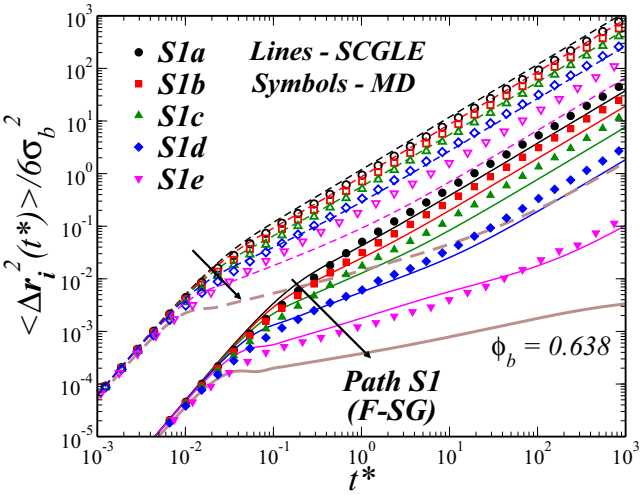

FIG. 7. MSD for the large (solid symbols and solid lines) and small particles (open symbols and dashed lines) along path *S1* (as indicated) obtained from MD simulations (symbols) and the SCGLE theory (lines).

For instance, one observes that, at intermediate and long times, $W_s^*(t)$ (open symbols) only decreases by a factor of approximately one order of magnitude along path *S1*. Instead, $W_b^*(t)$ (solid symbols) decreases by more than two orders of magnitude and exhibits an increasingly extended subdiffusive regime at intermediate times with larger ϕ_b.

In summary, the dynamics of the binary mixture approaching the F-SG transition was outlined with the assistance of SCGLE, MD, and DDM experiments. In the self-dynamics of the system, only the large spheres display arrest. The small particles, instead, undergo long-ranged transport even if the mixture as a whole is in a nonergodic state. In contrast, on the level of collective dynamics, one observes that the two species display nonergodic behavior, with the small spheres following the dynamical arrest of the large ones, and with modulations in the wave-number dependence of the dynamics due to the frozen structure of the big spheres. This indicates that the small particle's density fluctuations cannot decay independently from the very slow dynamics of the frozen background formed by the large species. Thus, the F-SG transition indeed is induced by the arrest of a single species, the large particles which, however, lead also to the arrest of the collective motion of the small spheres, but still allowing individual small particles to explore the voids left by the large particles.

B. Dynamics of the F-DG transition

We now consider the F-DG transition. For this, theory and simulation results for constant $\phi_s = 0.2$ and increasing ϕ_b, i.e., along path *D1*, are first discussed. Figures 8(a) and 8(b) report the behavior of the SISF along this path, and at fixed $q^* = 7.18$. Different from the case of approaching the F-SG transition, one notices that the relaxation patterns displayed by F_b^S and F_s^S are now rather similar. The latter still show the faster decay, but upon increasing ϕ_b, both SISF slow down by a similar factor. No signature of a stretched relaxation in F_s^S is observed, and F_b^S now decays within the observation time window. These results reflect thus the *lubricating* effect of the large enough fraction of small particles on the big particles' dynamics, as suggested by previous experimental studies [11,20,26–28,31,32] (compare, for instance, the behavior of F_b^S at the two state points *S*1*e* [Figs. 2(a) and 2(b)] and *D*1*d*, both represented by down triangles, and both satisfying $\phi_s + \phi_b = 0.65$).

The corresponding collective ISF are displayed in Figs. 8(c) and 8(d). For the large particles, f_{bb} behaves quite similar to F_b^S, and also decays faster in comparison to the behavior found along path *S1*. In contrast, f_{ss} differs from F_s^S and shows a qualitatively distinct behavior with respect to path *S1*. The collective ISF of the small species now rapidly shows a relaxation pattern that, from intermediate times onward, resembles that of the large particles f_{bb}. Approaching the F-DG transition, these correlation functions become essentially indistinguishable.

To test the influence of ϕ_s on the qualitative features observed in the collective dynamics approaching the double-glass scenario, we next consider another route in which ϕ_b is kept constant (at about 0.3) and ϕ_s is increased, i.e., path D2. Figure 9 shows the results for the measured f_{bb} and f_{ss} along

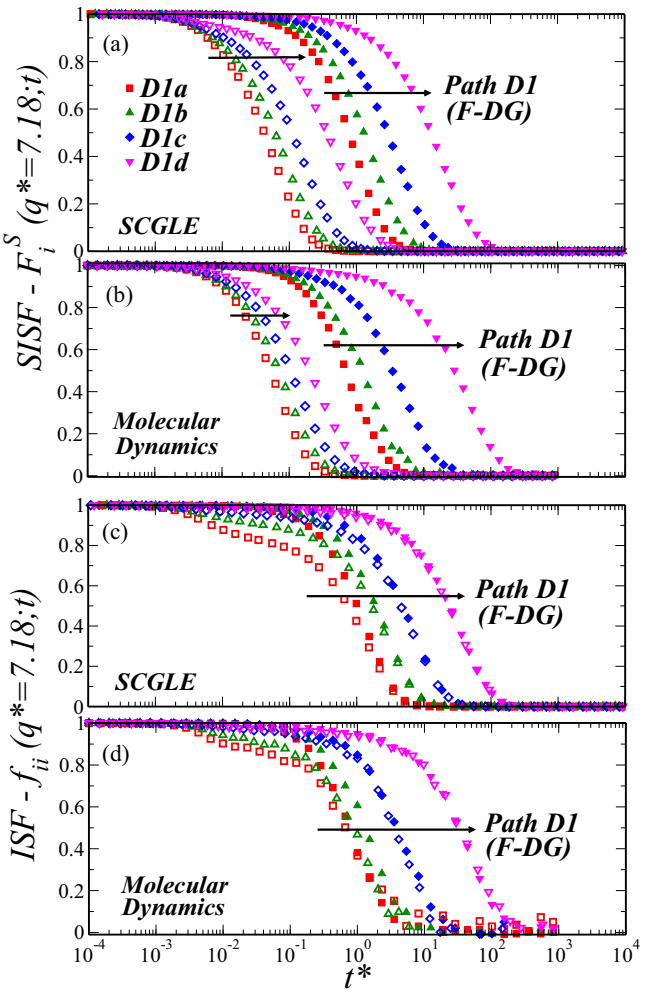

FIG. 8. Self- and collective-intermediate-scattering functions (SISF and ISF) of the large and small particles, calculated along the state points of path *D1* (as indicated), at fixed $q^* = 7.18$, as a function of the reduced time $t^* \equiv t/t_b^0$. (a) Results of the SCGLE theory for the SISF $F_b^S(q^* = 7.18, t^*)$ (solid symbols) and $F_s^S(q^* = 7.18; t^*)$ (open symbols). (b) Corresponding results obtained with event-driven MD simulations. (c), (d) Corresponding results for the ISF $f_{bb}(q^* = 7.18, t)$ and $f_{ss}(q^* = 7.18, t)$.

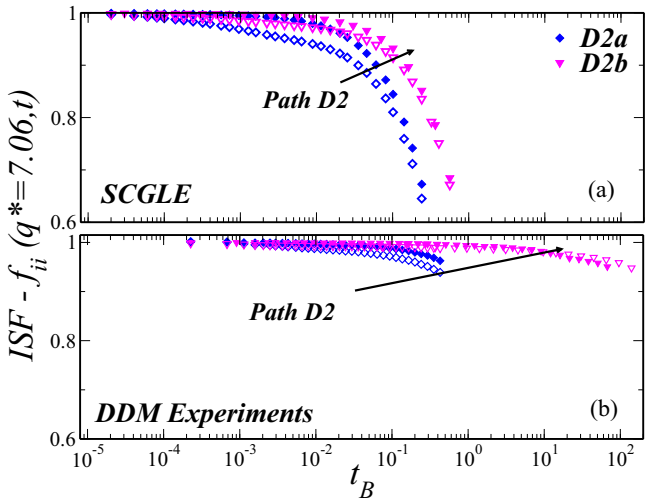

FIG. 9. Collective ISF of the large $f_{bb}(q^*, t)$ (solid symbols) and small $f_{ss}(q^*, t)$ (open symbols) particles, along path *D2* (as indicated), at fixed $q^* = 7.06$ as a function of the scaled time $t_B \equiv t/\tau_B$. The top panel displays predictions of the SCGLE and the bottom panel DDM measurements.

this path. Due to the limited measurement time (on the order of a day), the experimental data extend over a smaller time window. Thus, the final decay of both $f_{bb}(q, t)$ and $f_{ss}(q, t)$ is not accessible in the experiments. Nevertheless, the trends are compatible with the results of MD simulations along path *D1*, where the relaxation of f_{bb} and f_{ss} becomes slower and practically indistinguishable but now with increasing ϕ_s. Figure 9 also shows theoretical results for the states measured in DDM. They agree in the sense that the relaxation functions associated to the small and large particles resemble each other as the glass transition is approached. The theory predicts a much weaker variation in the final structural relaxation time between the two state points along this path than that observed in experiments. This could indicate that the glass-transition point predicted by the theory is located at a slightly higher packing fraction than corresponds to the experimental system. It could be a quantitative error of SCGLE, but also due to the differences between the experimental system and the binary HS model used in the theory, or uncertainties in the experimental determination of the volume fraction [54].

The fact that the results along paths *D1* and D2 share similar qualitative features again highlights that the dynamical arrest scenario that is associated to the F-DG transition does not qualitatively change if the path used to approach the transition is varied.

As above, we also study the q^* dependence of the collective dynamics for the most concentrated samples, i.e., *D1d* and *D2b* (Figs. 10 and 11, respectively). One notices that, for values $q^* \lessapprox 7$, the decay of both f_{bb} and f_{ss} is very similar and essentially independent of q^* in MD and experiments. In the theory, only a small and rather irrelevant acceleration with increasing q^* is observed. For $q^* > 7$, the relaxation time of both ISF continues monotonically and only moderately decreasing, but a slightly different initial relaxation is observed in f_{ss}, followed by an inflection point and transient plateaus [in the experiments this effect appears shifted to larger $q^*(\approx 14)$ with respect to MD and theory]. Furthermore, the height of these plateaus is significantly larger than those appearing at the state points *S1e* (Fig. 4) and *S2c* (Fig. 5), thus suggesting weak structural effects on the collective dynamics toward the F-DG transition.

Finally, let us refer to the behavior of the MSD along path *D1*. This is shown in Fig. 12. For the state points we considered, the small-particle MSD slows down by about one decade in the final mobility, while in the case of the large particles only by roughly a factor of 50. This is to be contrasted with the conditions found along path *S1*, Fig. 7, where a similar slowing down of a factor of 10 in the small-particle MSD is caused by a much more drastic effect in the large-particle self-dynamics (amounting to a factor of 500).

In summary, the results of this section reveal a different scenario toward the F-DG transition, where the self-dynamics of the large and small spheres becomes slower simultaneously.

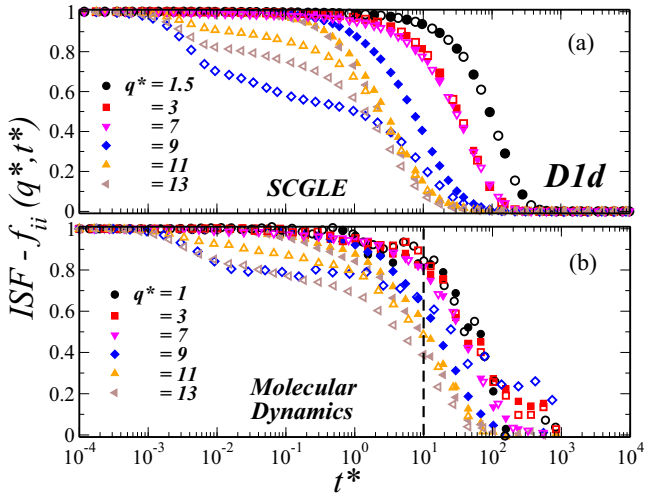

FIG. 10. Collective ISF for the large $f_{bb}(q^*, t^*)$ (solid symbols) and small particles $f_{ss}(q^*, t^*)$ (open symbols), at the state point $D1d$, for different wave numbers q^* (as indicated) as a function of the reduced time t^*, obtained from the SCGLE theory (upper panel) and MD (lower panel). The vertical dashed line in the lower panel indicates $t^* = 10$ at which the values $f_{ii}(q^*, t^* = 10)$ were extracted for the comparison in Fig. 15(b).

The collective dynamics also shows similar trends for the two species at all the relevant length scales, and displays weak structural effects. These results suggest that both big and small spheres become arrested in the self-dynamics and collective dynamics toward the DG domain.

C. Comparison of the dynamics toward the F-SG and F-DG transitions

The self-dynamics and collective dynamics approaching the F-SG and F-DG transitions have been described above and

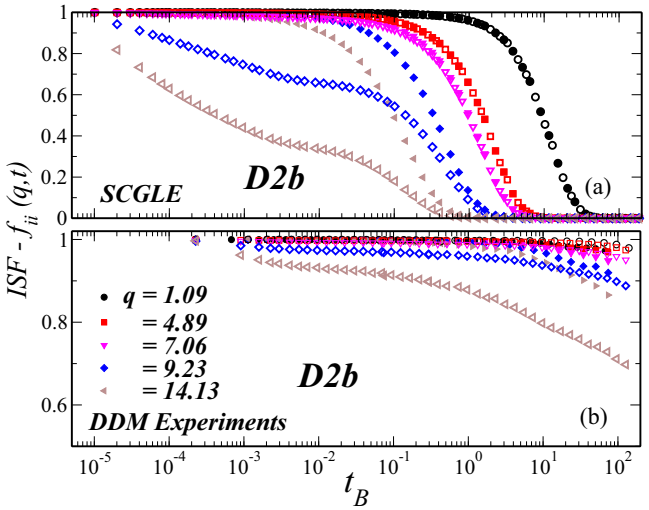

FIG. 11. Collective ISF for the large $f_{bb}(q^*, t^*)$ (solid symbols) and small, $f_{ss}(q^*, t^*)$ (open symbols) particles, at the state point $D2b$, for different wave numbers q^* (as indicated) as a function of scaled time t_B. The top panel displays predictions of the SCGLE theory and the bottom panel DDM measurements.

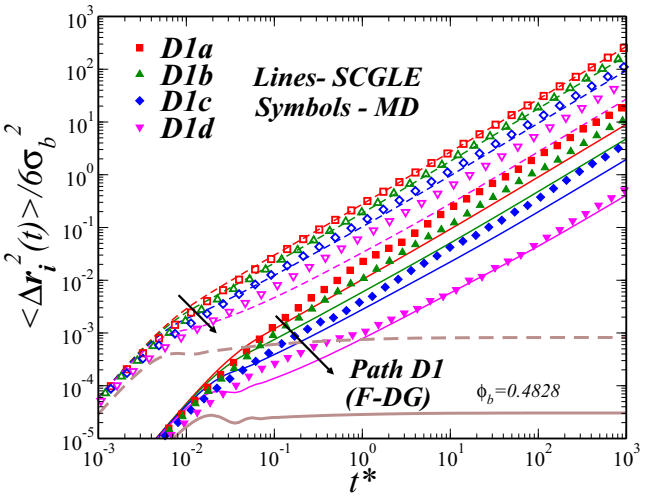

FIG. 12. MSD for the large (solid symbols and solid lines) and small particles (open symbols and dashed lines) along path $D1$ (as indicated) obtained from MD simulations (symbols) and the SCGLE theory (lines).

will now be compared. For this, notice that for each state point along path $D1$, there is a corresponding point along path $S1$ having the same total volume fraction ϕ, but a different composition $x_s \equiv \phi_s/\phi$. To highlight the corresponding samples, in Figs. 2 (path $S1$) and 8 (path $D1$) we have used the same symbols to represent those state points with the same ϕ.

In Fig. 13, the evolution of the self-dynamics along both paths is compared in terms of the ϕ dependence of the structural relaxation times (also called α-relaxation times) τ_i^S, approximated here as $F_i^S(q^* = 7.18, \tau_i^S) = 1/e$. For samples with the same ϕ, the relaxation time of the small species is moderately larger along path $D1$ ($\phi_s = 0.2$) than path $S1$ ($\phi_s = 0.05$), but τ_s^S displays essentially the same overall behavior in the ϕ range considered. This comparison, however, does not take into account the distinct relaxation patterns that

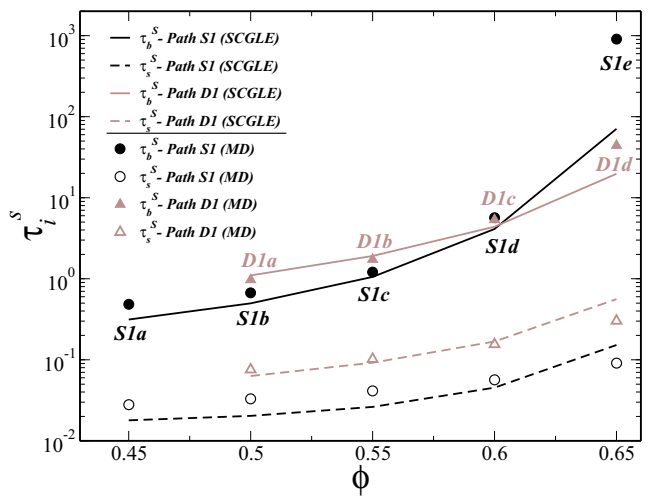

FIG. 13. Self-α-relaxation times of large (solid symbols, solid lines) and small particles (open symbols, dashed lines) along paths $S1$ and $D1$ as a function of the total volume fraction ϕ. Symbols represent MD data and lines SCGLE results, as indicated.

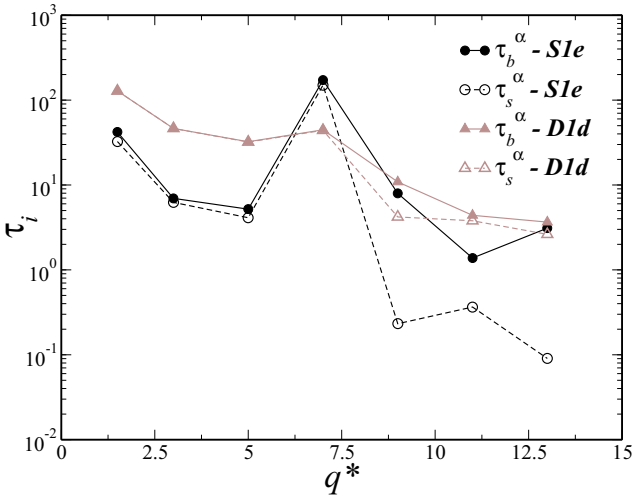

FIG. 14. Collective α-relaxation times of large (solid symbols, solid lines) and small (open symbols, dashed lines) particles as a function of reduced wave number q^*, at the state points $S1e$ and $D1d$, as indicated, predicted by the SCGLE theory.

are observed in F_s^S along paths *S1* [Figs. 2(a) and 2(b)] and *D1* [Figs. 8(a) and 8(b)]. The different nature of the slowing down is revealed by considering the large-species' dynamics in addition. For $\phi < 0.6$, the difference in the relaxation of F_b^S along both paths is smaller in comparison to the case of the small spheres, with τ_b^S being slightly larger along path *D1*. A crossover, however, is observed at $\phi \approx 0.6$ and, for higher $\phi(=0.65)$, τ_b^S becomes noticeable larger along path *S1*. Overall, for the range of packing fractions ϕ shown in Fig. 13, a slowing down of the dynamics (as set by the large particles) to a factor of about 1000 along path *S1*, is compared to only a factor of about 50 along path *D1*. In other words, a similar effect on the small-particle dynamics corresponds to a much stronger slowing down of the large particles along path *S1* than along path *D1*. This is consistent with the picture that toward the F-SG transition, the slowing down of the small species is driven by the large particles, whereas toward the F-DG transition both species undergo an arrest transition. The theoretical results shown in Fig. 13 are in reasonable agreement with the MD simulation data; except for the structural relaxation time of the large spheres at the highest ϕ, where the theory predicts a less drastic splitting for the relative slowing down of the large and that of the small particles, i.e., it underestimates the differences in the two transition scenarios for the specific paths chosen here.

To compare the collective dynamics close to the F-SG and F-DG transitions, we similarly consider collective relaxation times defined by $f_{ii}(q^*, t^* = \tau_i) = 1/e$, for different q^* values, and at the state points $S1e$ and $D1d$, respectively (Fig. 14). For $q^* \leqslant 7.18$, the relaxation times of the small and large particles are strongly coupled for both compositions, with path *D1* displaying the slower relaxation for $q^* < 7$ and a crossover at $q \approx 7.18$ similar to the behavior of τ_i^S. At $q^* > 7.18$ and large x_s (i.e., many small particles, $D1d$) the relaxation of each species is essentially the same, which reflects a more pronounced contribution of the small-particles dynamics to the slowing down of the mixture. In contrast, if the fraction of small particles is decreased (small x_s) and the F-SG is close ($S1e$), one observes two separate relaxation times, with the small species displaying a faster decay reflecting their ability to explore the local environment.

D. Nonergodicity parameters and localization lengths

The previous results provide the cornerstone elements to develop a general and unified description of the glassy dynamics in highly asymmetric HS binary mixtures. In order to systematically analyze our observations, we now use the SCGLE and subsequently compare its results to simulations and experiments. Our previous discussion demonstrates that this theoretical framework reasonably describes the features observed in MD and DDM upon approaching dynamical arrest. Thus, we employ the theory to construct the GT lines in the parameter space and to summarize the structural and dynamical features of the single- and double-glass states. This is particularly helpful because a precise determination of GT points from experiments and simulations is notoriously difficult since all the samples close to a transition tend to show severe instabilities and display history dependence. A common protocol consists in estimating these points from the divergence of the α-relaxation times τ_i^S or, alternatively, from an extrapolation of the long-time diffusion coefficients D_i^L. Nevertheless, these methods are prone to errors since they intrinsically involve large uncertainties in the choice of the specific extrapolation function and the fit range.

We consider the predictions for the GT lines of a HS binary mixture, with $\delta = 0.2$, provided by the SCGLE. Let us briefly remind some technical details regarding the determination of GT lines within this theoretical framework. The theory provides closed equations for the *nondecaying* components of the collective ISF, commonly referred to as nonergodicity parameters (NEP) [10,11] and defined as $f_{ii}^\infty(q) \equiv \lim_{t\to\infty} f_{ii}(q,t)$ and for the parameters γ_i, related to long-time limit of the MSD of species i, $\lim_{t\to\infty}\langle[\Delta\mathbf{r}_i(t)]^2\rangle$ [37]. The quantities γ_b^{-1} and γ_s^{-1} play the role of order parameters in the determination of the ergodic-to-nonergodic transitions of the mixture. Both are zero in a fully ergodic fluid state (F), leading also to $f_{bb}^\infty(q) = f_{ss}^\infty(q) = 0$. Any other solution indicates partial or total loss of ergodicity. For example, one finds a region (SG) in the (ϕ_b, ϕ_s) plane characterized by the condition $\gamma_b^{-1} \neq 0$, $\gamma_s^{-1} = 0$, $f_{bb}^\infty(q) \neq 0$, and $f_{ss}^\infty(q) \neq 0$. This condition describes, thus, states where the *self*-dynamics of the small particles remains ergodic, whereas that of the large species becomes arrested, and where the collective ISF of both species undergo arrest. Similarly, another region (DG) is found where both order parameters and all $f_{ii}(q)$ are different from zero. Hence, based on the SCGLE, three different states of the mixture can be distinguished: a fluid, where both species diffuse, a double glass, in which both components become arrested in the collective and self-dynamics, and a single glass, where the collective dynamics of the system undergoes a GT, but with the small particles still diffusing through the voids left by the large spheres. The locus of the boundaries between these regions defines the transition lines shown in Fig. 1.

The two different boundaries enclosing the ergodic region F describe the following: The transitions from a fluid state to a single-glass state (i.e., the F-SG transition), represented

by the dashed line in Fig. 1; and the transitions from a fluid state to a double-glass (F-DG) which corresponds to the solid line in the same figure. The F-SG line runs from the state point ($\phi_b = 0.582,\ \phi_s = 0$), i.e., *the GT point in the absence of small particles*, and represents a monotonically increasing function of ϕ_s, which indicates that the total volume fraction of the mixture to reach the F-SG increases with ϕ_s. Therefore, a single glass state can be *melted* upon the addition of small particles [26]. As mentioned before, the previous results for samples *S*1*e* (MD), *S*2*c*, and *S*3*a* (DDM) are consistent with this prediction. In contrast, the F-DG line corresponds to a distinct type of transition, where the total volume fraction for the GT becomes a monotonically decreasing function of ϕ_s and which intersects the vertical axis of Fig. 1 at the point ($\phi_b = 0,\ \phi_s = 0.582$), i.e., *the GT point in the absence of big particles*. Recall that the samples *D*1*d* and *D*2*b* (corresponding to $\phi = 0.65$ and 0.6, respectively) displayed essentially the same dynamics and, thus, are in qualitative agreement with this scenario. In the limit of small ϕ_b, this line describes a special type of *asymmetric* glass, where the large particles are localized in a glass of small spheres [36,37], as already observed in previous experimental work [30–32].

Moreover, a third transition (dashed-dotted line in Fig. 1) separates the SG-DG regions. This transition describes the dynamical arrest of the small particles in the arrested large spheres. We have not considered this transition in the MD or DDM since this would require to perform extremely demanding simulations and experiments due to the very slow dynamics with pronounced aging effects [33]. Notice, however, that the SCGLE predicts that samples along path *S3* belong to the SG domain, in agreement with the experimental conditions reported in Ref. [33].

Figure 15 illustrates the different structural features associated with the distinct GTs, as they are expected from the predictions of the SCGLE theory. We show the NEP of the big, $f_{bb}^{\infty}(q^*)$, and small, $f_{ss}^{\infty}(q^*)$, particles at three points located on the F-SG, F-DG, and SG-DG lines, respectively, as a function of the reduced wave number q^*. To allow for a comparison with MD data, we have chosen the points on the F-SG and F-DG transition lines that correspond, respectively, to the crossing points with paths *S1* and *D1*. Similarly, we have considered the extrapolation of path *S3* with the SG-DG line for a comparison with DDM results.

For the point at the intersection of the extended path *S1* with the F-SG line [Fig. 15(a)], one observes an oscillatory behavior in both $f_{bb}^{\infty}(q^*)$ and $f_{ss}^{\infty}(q^*)$, associated with the modulations of the structure factor of the big species $S_{bb}(q^*)$. The two NEP appear coupled and they are essentially identical up to $q^* \approx 7.18$, which approximately corresponds to the location of the main peak of $S_{bb}(q^*)$. Thus, at large length scales, the collective dynamics of the small spheres is controlled by the confinement by the large particles. For $q^* > 7.18$, oscillations are still present, but become decoupled. The NEP cease to oscillate and decay to nearly zero at values $q^* \approx 20$ in the case of $f_{ss}^{\infty}(q^*)$ and $q^* \approx 30$ for $f_{bb}^{\infty}(q^*)$. This indicates that, at smaller length scales, the small spheres can still explore the local environment.

In contrast, for the point at the intersection of the extended path *D1* with the F-DG transition line [Fig. 15(b)], the theory predicts a different behavior. Both $f_{bb}^{\infty}(q^*)$ and $f_{ss}^{\infty}(q^*)$ remain

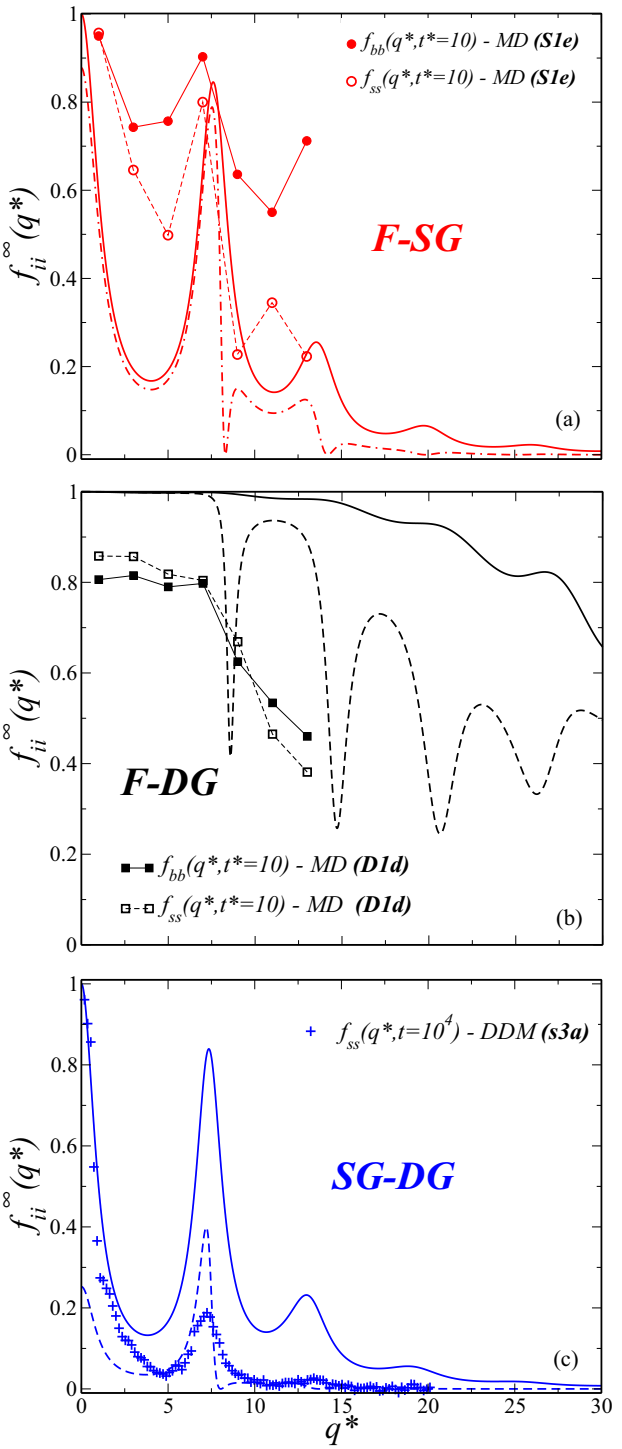

FIG. 15. *Nonergodicity* parameters (NEP) of the large particles $f_{bb}^{\infty}(q^*)$ (solid lines) and of the small particles $f_{ss}^{\infty}(q^*)$ (dashed lines) as a function of the reduced wave number q^* predicted by the SCGLE formalism (a) at the intersection of path *S1* with the F-SG transition line; estimates of the NEP obtained from MD simulations for $f_{bb}(q^*, t^* = 10)$ (solid symbols) and $f_{ss}(q^*, t^* = 10)$ (open symbols) at the state point *S*1*e* are also displayed, (b) at the intersection of path *D1* with the F-DG transition line; estimates of both NEP obtained from MD simulations at the state point *D*1*d* are also shown, (c) at the intersection of path *S3* with the SG-DG transition line; experimental data from Ref. [33] for $f_{ss}(q^*, t = 10^4)$ (+ symbols) at the state point *S*3*a* are also displayed.

close to unity and without oscillations for $q^* \leqslant 7.18$, thus indicating the tendency of both ISF to develop higher plateaus with respect to the previous case. For $q^* > 7.18$, the NEPs behave different and large oscillations appear in $f_{ss}(q^*)$. Also, a larger spectrum of nondecaying components in the ISF of both species is observed up to $q^* \approx 150$ (not shown).

In Fig. 15(c), the SCGLE predictions for the behavior of the NEP at the intersection of the SG-DG transition line with the extended path *S3* are shown. The behavior is qualitatively similar to that observed at the F-SG transition, but $f_{ss}(q^*)$ is noticeably smaller than $f_{bb}(q^*)$ for $q^* \leqslant 7.18$, and becomes nearly zero for $q^* > 7.18$. Hence, at this transition the small particles become trapped in voids created by big particles, thus resembling a localization transition in random porous media [53].

Due to the technical reasons explained above, simulations and experiments could not be performed at the GT. However, the dynamics observed in both techniques close to the GT is compatible with these theoretical predictions. Figure 15 also shows estimates of the NEP obtained from MD and DDM. As estimates, we use values of the ISF at an intermediate time that is long enough to be outside the initial decay but short enough to not yet probe the final structural relaxation toward zero. As shown in Figs. 15(a) and 15(b), the data extracted from the state points *S*1*e* (Fig. 4) and *D*1*d* (Fig. 10) follow the qualitative trends discussed above for the F-SG and F-DG transition lines, respectively. Along path *S1*, the simulations confirm much lower plateau values for the small-particle dynamics than the large-particle dynamics, while along path *D1* the nonergodic contributions from both species are roughly identical. To probe the features of the SG-DG transition, we estimate plateau values for $f_{ss}^{\infty}(q^*)$, obtained from DDM experiments (Fig. 6, at $t = 10^4$ s) along path *S3*. Here, the state *S*3*a* was chosen as a proxy because the data for *S*3*c* proved to be too noisy. Given these restrictions, the experimental data are in good qualitative agreement with the theoretical prediction, as shown in Fig. 15(c).

We finally discuss the behavior of the long-time plateau of the MSD, i.e., the parameters γ_b and γ_s. In an ordinary HS glass, its height indicates the maximum possible displacement inside a *nearest-neighbors* cage [31,32]. The square root of this value is called localization length l_i and is a measure of the local confinement. In Fig. 16, the behavior of the localization lengths calculated along the F-SG and F-DG lines is reported. For the F-SG line, the normalized localization length $l_b^* \equiv l_b/\sigma_b$ of the big spheres (solid diamonds) is found to be $l_b^* \approx 10^{-1}$ (notice that along this line the total volume fraction of the mixture increases). Hence, their characteristic *cage size* corresponds to approximately 10% of their diameter, a typical feature of an ideal glass of HS. On the other hand, the normalized localization length of the small particles, $l_s^* \equiv l_s/\sigma_b$, is infinite, indicating that the latter ones are not localized and diffuse (a feature not observed for a small degree of asymmetry [28]). These results are in qualitative agreement with the scenario for the self-dynamics provided by the MD simulations (Figs. 2 and 7).

At the intersection of the F-SG and F-DG lines, l_b^* discontinuously jumps from $\sim 10^{-1}$ to $\sim 10^{-2}$ (solid squares) and l_s^* becomes suddenly finite with a value $l_s^* \sim 10^{-1}$ (open squares). This indicates that along the F-DG line both species

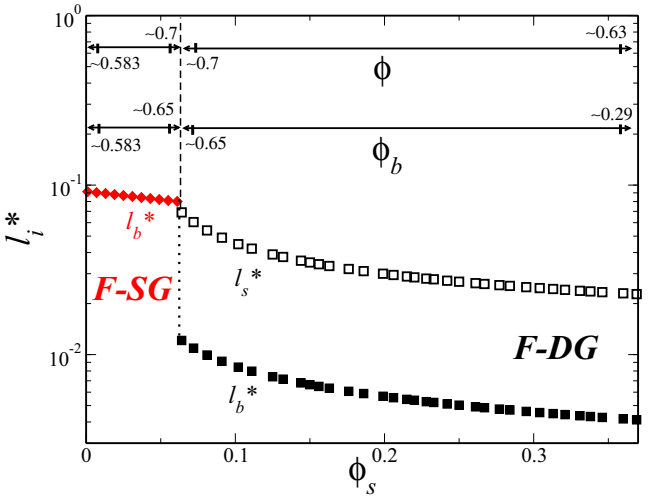

FIG. 16. Normalized localization lengths l_b^* (solid symbols) and l_s^* (open symbols) of the large and small particles, respectively, as function of the volume fraction of small particles ϕ_s, calculated with the SCGLE formalism along the two transition lines enclosing region F (Fig. 1).

are localized, with the small particles being less localized than the large ones. The latter become even more localized than along the F-SG transition in agreement with previous experimental results [31,32] (see Sec. 2 of Appendix C). As mentioned before in this case, the total volume fraction decreases when going from the intersection point toward the point ($\phi_b = 0$, $\phi_s = 0.582$). Both l_b^* and l_s^* become smaller with decreasing ϕ and increasing ϕ_s, which implies that the cage size along the F-DG line is controlled by the small spheres.

Despite this qualitative agreement between SCGLE, MD, and DDM results, one should also refer to the quantitative differences found in comparison to additional experimental data. For instance, for a higher degree of asymmetry ($\delta = 0.1$) the theory less accurately determines the locus of the GT lines [29,30] (see Fig. 18 in Appendix C). Nevertheless, the SCGLE results remain in qualitative agreement with the main physical scenario emerging from such experimental characterizations, and the theory reproduces also the behavior observed for measurements at similar degree of asymmetry [31]. We believe that these differences are due to the very simplified character of the theory and the approximations applied in the determination of the static structure factor [50,51], as well as polydispersity, residual charges, and other effects present in the experimental samples, in particular, hydrodynamic interactions (HI). However, the consistent picture of the arrest scenarios that emerges from our discussion of both MD simulation data (where no HI are present by definition) and experiments on colloidal suspensions suggests that HI do not change the qualitative aspects of the different glasses found in binary hard-sphere mixtures.

III. CONCLUDING REMARKS

By combining experiments, molecular dynamics simulations, and theoretical calculations based on the SCGLE theory,

we have presented a general and consistent physical description of glassy dynamics in highly asymmetric binary mixtures of hard spheres. Two fundamentally different glass states, the single glass and the double glass, as well as the corresponding transitions from the fluid were examined and characterized in terms of the experimentally accessible scattering functions, namely, the collective ISF and the tagged-particle SISF. Both glasses lead to dynamical arrest of the large particles, and, for the case of the single glass upon further densification, eventually also the small particles. Hence, both transitions are related to distinct signatures in the dynamics.

Below a certain volume fraction of small spheres, a transition to a single glass is observed. The slowing down of the dynamics of the system is dominated by the large species, whose SISF and collective ISF indicate an approach to arrest with the typical characteristics of the well-known glass transition of hard spheres. At large length scales, the collective ISF of the small particles follows a pattern dictated by the structure and dynamics of the big species, while at short length scales appears decoupled. Moreover, the self-dynamics of the small spheres does not arrest, but resembles the behavior of a fluid embedded in a heterogeneous medium, including a pronounced stretched decay in the relaxation functions at long times. In this regime, we find that the overall volume fraction to reach the glass transition becomes larger with increasing volume fraction of small particles, i.e., the small spheres serve to fluidize the mixture.

In the double-glass transition, both species show a broadly similar approach to dynamical arrest. In consequence, the same amount of slowing down in the large-particle dynamics is accompanied by a much more pronounced concomitant slowing down of the small particles than in the approach to the single-glass transition. The strong coupling between the two species is observed at essentially all length scales, i.e., the microstructure and dynamics is determined by both particles. Consistent with this behavior, in this regime the overall packing fraction required for dynamical arrest becomes smaller with increasing packing fraction of the small particles.

Our characterization is based on the species-resolved collective and tagged-particle scattering functions, the ISF and the SISF, respectively. Broadly speaking, both intermediate scattering functions measure how a many-body system changes with time on a given length scale. The ISF probes the changes in the overall particle arrangement, while the SISF is a measure of individual motion. A typical case is that the motion of individual particles already suffices to induce a loss of overall structure, and in these conditions the SISF and the ISF decay roughly equally. This is, essentially, the case for the double glass.

If, however, as in the single glass, some part of the overall structure remains intact even though individual particles are able to move, the SISF of the small spheres decays faster than that of the large spheres, and also faster than the collective ISF of the two species. In this sense, a decoupling between self-dynamics and collective dynamics arises toward the single glass. Note that this implies that the remnant structure of the large particles inhibits an overall structural relaxation of the large- as well as small-particle structure, and thus no decoupling is observed between the ISF of the two species. Therefore, a quantification of small-particle mobility in the single glass requires the measurement of the SISF of this species.

As predicted by the SCGLE, a collective quantity that allows to distinguish the single and double glass is the propagator $\Psi_{\alpha\beta}(q,t)$, defined by $\mathbf{\Psi}(q,t) \equiv \mathbf{F}(q,t) \cdot \mathbf{S}^{-1}(q)$ (where bold symbols indicate matrices in the species indices). The quantity $\Psi_{\alpha\beta}(q,t)$ can be interpreted as the effect of the static structure associated to the species β on the collective dynamics of the species α. In the double glass, all entries of $\mathbf{\Psi}(q,t)$ remain finite [37], whereas in the single glass only the $\Psi_{\alpha\beta}$ associated with $\beta = b$ remain finite (positive or negative) whereas those associated with $\beta = s$ relax to zero (see Sec. 3 of Appendix C). This indicates that in the single glass, the big-particles *static* structure affects the glassy (long-time) dynamics of the small species, but the glassy dynamics of large spheres is not influenced by the static structure of the small particles (but only by their dynamics).

However, as discussed above, even in the collective ISF distinct features arise due to the length-scale-dependent microstructure, and therefore wave-vector resolved experiments provide valuable information to distinguish the different glassy regimes of binary mixtures with disparate length scales. A mere discussion of structural relaxation times at a single length scale does not reveal the full information on the different transition scenarios. Experiments that are able to resolve the dynamics of both the large and the small species are required to fully characterize the different glassy states. This also points to the fact that effective single-species models where the motion of one species (typically the small one) is integrated out to yield an effective potential, are not sufficient to understand the evolution from single to double glass.

Our simulations and the experimental data presented above provide the first thorough validation of the SCGLE theory of glass transitions in binary mixtures. Using the SCGLE theory as an experimentally validated basis, we have constructed a generic state diagram of size-disparate binary hard-sphere mixtures. The effects are generic to the appearance of competing length scales in the system, and therefore should be applicable also to a wider range of colloidal (non-hard-sphere) mixtures and also polymeric or protein solutions with different length scales and possibly also certain metallic alloys.

Recently, the SCGLE approach has been extended to a *nonequilibrium* (NE-SCGLE) theory of irreversible processes in liquids out of thermal equilibrium [55–57]. The NE-SCGLE provides a microscopically founded tool for the understanding of essential characteristics of the aging kinetics of solidifying liquids or the processing-protocol dependence of amorphous solids [58]. In this regard, the NE-SCGLE theory has proven to be advantageous in its ease of generalization and application over more rigorous (and technically involved) theories, for example, those based on MCT. The results that we present here are thus an important step in extending SCGLE to the description of nonequilibrium transformations in amorphous mixtures, which are the systems of applicational relevance. We hope that this provides a basis to facilitate the rational design of amorphous materials and eventually the industrial processes involved in their fabrication.

ACKNOWLEDGMENTS

This work was supported by the Consejo Nacional de Ciencia y Tecnología (CONACYT, Mexico) through Grants No. 242364, No. 182132, No. 237425, No. 358254, No. 287067, No. FC-2015-2/1155, No. LANIMFE-279887-2017, and No. CB-2015-01-257636. L.F.E.A. acknowledges financial support from the German Academic Exchange Service (DAAD) through the DLR-DAAD programme under Grant No. 212. P.L. and S.U.E. acknowledge support by the German-Israeli Foundation (Grant No. I-1345-303.10/2016). R.C.P. acknowledges the financial support provided by Marcos Moshinsky Foundation, the University of Guanajuato (Convocatoria Institucional de Investigación Científica 2018), and the Alexander-von-Humboldt Foundation during his stay at the Henrich Heine University, Düsseldorf.

APPENDIX A: SIMULATIONS

1. Technical details

We have carried out event-driven molecular dynamics (MD) simulations for a HS binary system with size asymmetry $\delta \equiv \sigma_s/\sigma_b = 0.2$. We have simulated N_b big spheres and N_s small spheres in a volume V. We have investigated the dynamics of the mixture following two different paths in the plane (ϕ_b, ϕ_s), representing fixed $\phi_s = 0.05$ (for path *S1* in Fig. 1) and $\phi_s = 0.2$ (for path *D1*), respectively, and increasing ϕ_b toward the dynamical arrest transitions enclosing the fluid region F predicted by the SCGLE theory.

For path *S1*, we have simulated a system of fixed $N_b = 200$ big particles and a variable number of small particles N_s. More specifically, we have considered the following values for each point investigated (Fig. 1): (*S*1*a*) $N_s = 3125$, (*S*1*b*) $N_s = 2778$, (*S*1*c*) $N_s = 2500$, (*S*1*d*) $N_s = 2273$, and (*S*1*e*) $N_s = 2083$. For each state point, the size of the cubic simulation box was adjusted, together with N_s, in order to match ϕ_b. Along path *S1*, 10 different *seeds* (realizations) of the system have been used to explore the available phase space and to improve statistics. For the points *S*1*a*–*S*1*d* we have used a waiting time $t_w^* = 10^3$, whereas for point *S*1*e* we let $t_w^* = 10^4$ in order to avoid aging effects.

For path *D1*, we have simulated $N_b = 100$ big particles and (*D*1*a*) $N_s = 8333$, (*D*1*b*) $N_s = 7143$, and (*D*1*c*) $N_s = 6250$ small particles. For the state point *D*1*d*, we have considered $N_b = 150$ and $N_s = 8333$. Along path *D1*, only five different *seeds* were considered for each state point and a waiting time $t_w^* = 10^3$.

In the simulations, the unit of length is defined by the diameter of the large particles σ_b and the unit of mass is defined as the mass of the big particles M_b. The mass densities $\rho_\alpha^M \equiv M_\alpha/v_\alpha$ $[v_\alpha = 4\pi(\sigma_\alpha/2)^3/3,\ \alpha = s, b]$ are set equal to define the mass of the small particles. In the beginning, the velocity distribution is *updated* in order to fix the velocity of the center of mass of the system to zero. Thus, setting $k_B = 1$, the unit of time is defined from the equipartition theorem $\langle v^2\rangle = 3k_BT/2M_{\text{c.m.}}$. Periodic boundary conditions were employed in all directions. Finally, in order to generate nonoverlapping initial configurations, a soft standard MD with repulsive short-range potential and decreasing temperature was implemented [59]. This soft-core MD starts from a completely random initial configuration.

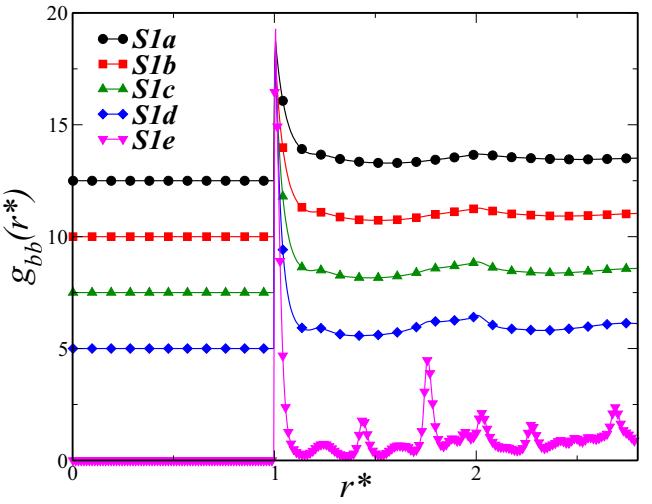

FIG. 17. Evolution of the radial distribution function $g_{bb}(r^*)$ along the state points in path*S1* obtained from MD simulations as indicated. The curves are vertically shifted for clarity and $r^* \equiv r/\sigma_b$.

2. Comparison of SCGLE theory and molecular dynamics

The SCGLE formalism is a theoretical framework to describe the dynamics of *colloidal* mixtures, i.e., dynamics originating from the Brownian nature of the microscopic particle motion. In our work, the SCGLE analysis is compared with results of MD simulations for HS, which are based on the Newtonian character of the individual particle motion and hence rather represent the motion of atoms. The long-time dynamical equivalence between a colloidal and an atomic liquid that share the same interparticle potential is well established [60–63]. In contrast, a fundamental difference appears in the short-time dynamics, colloidal motion is diffusive at all relevant timescales, whereas atoms show a crossover from ballistic to diffusive behavior after a few particle collisions. In a recent contribution [52], a SCGLE theory for the dynamics of multicomponent atomic fluids has been derived. When complemented with a Gaussian approximation, the resulting theory provides a reasonable representation of the transition from ballistic to diffusive behavior in atomic liquids, allowing us to quantitatively compare theory and MD simulations. The details of this approach and its specific implementation are discussed in Ref. [52].

3. Radial distribution function along path *S*1

Aside from the slowing down of both self-dynamics and collective dynamics of the large spheres along path *S1* (Figs. 2 and 7), the MD simulations also revealed structural behavior similar to that of a highly amorphous material at the state point *S*1*e*. This is seen in the evolution of the radial distribution of the large species $g_{bb}(r)$ along the state points of path *S1* shown in Fig. 17.

APPENDIX B: EXPERIMENTS

1. Materials

We have studied dispersions of sterically stabilized PMMA particles of different diameters. For path *S3*, $\sigma_b = 3.1$ μm (polydispersity 0.07, not fluorescently labeled) mixed with particles of diameter $\sigma_s = 0.56$ μm (polydispersity 0.13, fluorescently labeled with nitrobenzoxadiazole). For paths *S2* and *D2*, $\sigma_b = 3.1$ μm (polydispersity 0.06, fluorescently labeled with Nile Red) mixed with particles of diameter $\sigma_s = 0.56$ μm (polydispersity 0.13, fluorescently labeled with nitrobenzoxadiazole). This resulted in a size ratio $\delta \approx 0.18$ for both systems. In all cases, the colloids were dispersed in a cis-decalin/cycloheptylbromide mixture that closely matches the density and refractive index of the colloids. We added salt (tetrabutylammoniumchloride) to obtain hard-sphere-like interactions [64,65]. The volume fraction ϕ_b of a sediment of the large particles was estimated to be $\phi_b = 0.65$ by comparing with numerical simulations and experiments [25,66,67], the uncertainty $\Delta\phi_b$ typically is 3% [54]. In order to mix stock dispersions with comparable dynamics and therefore distance from the glass transition, we have assumed the generalized Stokes-Einstein relation [68] to be valid, and therefore compared the linear viscoelastic moduli of the one-component dispersions of the two species. The volume fraction of the small particles was adjusted until the linear viscoelastic moduli, measured in units of the energy density $6k_BT/\pi{\sigma_b}^3$, were comparable to those of the large particles. The frequency was multiplied by the free-diffusion Brownian time $\tau_B = 3\pi\eta{\sigma_b}^3/k_BT$, where $\eta = 2.2$ mPa s is the solvent viscosity. Note that comparable rheological response and dynamics imply that the stock dispersions of large and small particles have a slightly different ϕ due to the different polydispersities. Samples with different total volume fractions ϕ and compositions, quantified by the fraction of small particles $x_s = \phi_s/\phi = 0.01, 0.05$, were prepared by mixing the one-component stock suspensions. We should mention that the experimental system used in this work could be employed in principle to study also the self-dynamics using a mixture of labeled and unlabeled particles of the same batch. However, one could not easily obtain batches of identical particles which are labeled and unlabeled. Such kind of experiments will be performed in future investigations.

2. DDM measurements and analysis

We used a Nikon A1R-MP confocal scanning unit mounted on a Nikon Ti-U inverted microscope, with a 60× Nikon Plan Apo oil immersion objective (NA = 1.40). Confocal microscopy images were obtained in a plane taken approximately 30 μm from the coverslip. Images with 512×512 pixels, corresponding to 107 μm×107 μm, were taken at two different rates: a fast rate of 30 frames per second to follow the short-time dynamics and a slow rate, between 0.07 and 0.33 frames per second (depending on sample), to follow the long-time dynamics. The maximum pinhole diameter of 255 μm was used. Time series of 10^4 images were acquired for 2 to 5 distinct volumes, depending on sample.

Details of the image analysis using the DDM approach to obtain the intermediate scattering function $f(q,t)$ have been reported previously [33,34]. For measurements along path *S2*, instabilities of the microscope setup, mainly caused by a slow drift of the stage, limited the maximum measurement time.

APPENDIX C: THEORETICAL ANALYSIS

1. Multicomponent SCGLE theory

The SCGLE theory of colloid dynamics and dynamical arrest was previously introduced [45,46,48] and further extended to mixtures [37,38,47]. It provides the time and wave-vector dependence of the relevant dynamical properties of a colloidal mixture. Details of the derivation of this theory and its application to colloidal model systems are provided in Refs. [37,38,47] and references therein. The theory is summarized by a set of self-consistent equations describing the time evolution of the matrix $\boldsymbol{F}(q,t)$, whose $\alpha\beta$ elements are the *partial* intermediate scattering functions (ISF), $[\boldsymbol{F}(q,t)]_{\alpha\beta} \equiv \langle n_\alpha(q,t) n_\beta(-q,0)\rangle$, with $n_\alpha(q,t) = \sum_{i=j}^{N_\alpha} \exp[i\mathbf{q}\cdot\mathbf{r}_j^{(\alpha)}(t)]/\sqrt{N_\alpha}$ being the Fourier transform of the local density of particles of species α, $n_\alpha(\mathbf{r},t) = \sum_{j=1}^{N_\alpha} \delta(\mathbf{r} - \mathbf{r}_j^{(\alpha)}(t))/\sqrt{N_\alpha}$, and where $\mathbf{r}_j^{(\alpha)}(t)$ denotes position of the jth particle of species α at time t. The initial value $\boldsymbol{F}(q,0)$ is thus the static structure matrix $\boldsymbol{S}(q)$, with elements $[\boldsymbol{S}(q)]_{\alpha\beta} = \langle n_\alpha(\mathbf{q}) n_\beta(-\mathbf{q})\rangle$, and constitutes one input needed to solve the SCGLE equations. In this contribution, we employ the Percus-Yevick (PY) approximation [50] combined with the Verlet-Weiss (VW) correction [51] to determine the matrix $\boldsymbol{S}(q)$ of a binary mixture of hard spheres (HS). The SCGLE also provides the time evolution of the self-part of $\boldsymbol{F}(q,t)$, referred to as self-ISF matrix $\boldsymbol{F}^S(q,t)$, and with elements defined as $[\boldsymbol{F}^S(q,t)]_{\alpha\beta} \equiv \delta_{\alpha\beta}\langle\exp[i\mathbf{q}\cdot\Delta\mathbf{r}_\alpha(t)]\rangle$, where $\Delta\mathbf{r}_\alpha(t)$ denotes the displacement of *any* of the N_α particles of species α over a time t and $\delta_{\alpha\beta}$ is the Kronecker's delta. Written in the Laplace domain, the SCGLE equations read as [37,47]

$$\boldsymbol{F}(q,z) = \{z\boldsymbol{I} + q^2\boldsymbol{D}\cdot[z\boldsymbol{I} + \boldsymbol{\lambda}(q)\cdot\Delta\hat{\boldsymbol{\zeta}}^*(z)]^{-1} \cdot\boldsymbol{S}^{-1}(q)\}^{-1}\boldsymbol{S}(q) \tag{C1}$$

and

$$\boldsymbol{F}^S(q,z) = \{z\boldsymbol{I} + q^2\boldsymbol{D}\cdot[z\boldsymbol{I} + \boldsymbol{\lambda}(q)\cdot\Delta\hat{\boldsymbol{\zeta}}^*(z)]^{-1}\}^{-1}, \tag{C2}$$

where $\boldsymbol{I}$ is the identity matrix $[\boldsymbol{I}]_{\alpha\beta} = \delta_{\alpha\beta}$, $\boldsymbol{D}$ and $\boldsymbol{\lambda}(q)$ are diagonal matrices defined as $[\boldsymbol{D}]_{\alpha\beta} \equiv \delta_{\alpha\beta}D_\alpha^0$, and $[\boldsymbol{\lambda}(q)]_{\alpha\beta} = \delta_{\alpha\beta}[1 + (q/q_\alpha^c)]^{-1}$, and with D_α^0 being the short-time self-diffusion coefficient of species α. The parameter q_α^c is an empirical cutoff wave vector written as $q_\alpha^c = aq_\alpha^{\max}$, in which $q_\alpha^{\max}$ denotes the position of the maximum of $S_{\alpha\alpha}(q)$, and $a > 0$ is the only free parameter, eventually determined by a calibration procedure [58].

The $\alpha\alpha$ element $\Delta\zeta_\alpha^*(z)$ of the diagonal matrix $\Delta\hat{\boldsymbol{\zeta}}^*(z)$ that appears in Eqs. (C1) and (C2) is the time-dependent friction function of particles of species α, given by [37,47]

$$\Delta\zeta_\alpha^*(t) = \frac{D_\alpha^0}{3(2\pi)^3}\int d\mathbf{q}\, q^2[\boldsymbol{F}^S(q,t)]_{\alpha\alpha}[\boldsymbol{h}(q)\cdot\sqrt{\boldsymbol{n}}\cdot\boldsymbol{S}^{-1}(q) \times\boldsymbol{F}(q,t)\cdot\boldsymbol{S}^{-1}(q)\cdot\sqrt{\boldsymbol{n}}\cdot\boldsymbol{h}(q)]_{\alpha\alpha}, \tag{C3}$$

where the q-dependent matrix $\boldsymbol{h}$ is given in terms of $\boldsymbol{S}$ by $\boldsymbol{h} = \sqrt{\boldsymbol{n}}^{-1}\cdot(\boldsymbol{S} - \boldsymbol{I})\cdot\sqrt{\boldsymbol{n}}^{-1}$, and with the elements of the matrix

$\sqrt{\boldsymbol{n}}$ defined as $[\sqrt{\boldsymbol{n}}]_{\alpha\beta} \equiv \delta_{\alpha\beta}\sqrt{n_\alpha}$. Thus, for a fixed point (δ, ϕ_b, ϕ_s) in the parameter space of a binary mixture of HS, one starts by determining the static structure matrix $\boldsymbol{S}(q)$ to further solve Eqs. (C1)–(C3), and hence to obtain the self- and collective ISF, and the mean-square displacement (MSD) of each species.

The SCGLE also provides equations for the long-time asymptotic values of the dynamical properties involved, $f^{\infty}_{\alpha\beta}(q) \equiv \lim_{t\to\infty} F_{\alpha\beta}(q,t)/S_{\alpha\beta}(q)$, $f^{\infty,S}_{\alpha}(q) \equiv \lim_{t\to\infty} F^S_\alpha(q,t)$, and $\gamma_\alpha \equiv [\lim_{t\to\infty} \Delta\zeta^*_\alpha(t)]^{-1} D^0_\alpha$, typically referred to as non-ergodicity parameters (NEP), and which play the role of order parameters for the determination of the *ergodic-nonergodic* transitions of the mixture [37]. The most fundamental of these results is the following equation for the asymptotic value of the mean-square displacement of species α, $\gamma_\alpha \equiv \lim_{t\to\infty}\langle[\Delta\mathbf{r}_\alpha(t)]^2\rangle$:

$$\frac{1}{\gamma_\alpha} = \frac{1}{3(2\pi)^3}\int d^3k\, k^2 \{\boldsymbol{\lambda}[\boldsymbol{\lambda} + k^2\boldsymbol{\gamma}]^{-1}\}_{\alpha\alpha} \times \{\boldsymbol{c}\sqrt{\boldsymbol{n}}\boldsymbol{S}\boldsymbol{\lambda}[\boldsymbol{S}\boldsymbol{\lambda} + k^2\boldsymbol{\gamma}]^{-1}\sqrt{\boldsymbol{n}}\boldsymbol{h}\}_{\alpha\alpha}, \tag{C4}$$

where $\boldsymbol{c}$ and $\boldsymbol{h}$ are, respectively, the direct and total matrices of correlation functions, thus related to $\boldsymbol{S}$ by $\boldsymbol{S} = \boldsymbol{I} + \sqrt{\boldsymbol{n}}\boldsymbol{h}\sqrt{\boldsymbol{n}} = [\boldsymbol{I} - \sqrt{\boldsymbol{n}}\boldsymbol{c}\sqrt{\boldsymbol{n}}]^{-1}$, and with $[\boldsymbol{\gamma}]_{\alpha\beta} \equiv \delta_{\alpha\beta}\gamma_\alpha$. Hence, for the case of the mixture, one can also use the matrix $\boldsymbol{S}(q)$ to solve Eq. (C4) for the two parameters γ_b and γ_s, and the corresponding equations for the diagonal components of the NEP, i.e., $f^{\infty}_{bb}(q)$, $f^{\infty}_{ss}(q)$, $f^{\infty,S}_{b}(q)$, and $f^{\infty,S}_{s}(q)$ [37]. At each state point, the dynamical state of the system can be then *classified* using the resulting values of these parameters.

At fixed δ, one can *scan* the subspace (ϕ_b, ϕ_s) calculating the NEP at each state point, and determine the regions where a dynamical transition in a subset, or in all these parameters, occurs. This procedure allows us to locate the boundaries between the dynamically arrested regions and the *ergodic* ones. For $\delta \lesssim 0.38$, one finds three main possibilities for the values of the NEP [37], namely, (i) γ_b and γ_s diverge, and $f^{\infty}_{bb}(q) = f^{\infty}_{ss}(q) = f^{\infty,S}_{bb}(q) = f^{\infty,S}_{ss}(q) = 0$, i.e., both species diffuse and the system is in a fully *ergodic* state (F); (ii) γ_b is finite, γ_s diverges, $f^{\infty}_{bb}(q) \neq 0$, $f^{\infty}_{ss}(q) \neq 0$, $f^{\infty,S}_{bb}(q) \neq 0$, and $f^{\infty,S}_{ss}(q) = 0$, indicating that the collective dynamics of both big and small particles becomes arrested, while the self-dynamics of the small spheres remains ergodic and, thus, they are still able to diffuse through the voids left by the large ones. This is referred to as a partially arrested state (SG); and (iii) all the NEP are finite, thus corresponding to a fully arrested state (DG). In Fig. 18, the result of this procedure for the case $\delta = 0.1$ is illustrated.

2. Assessment of the dynamical arrest diagram: SCGLE vs confocal microscopy experiments

To test the scenario summarized in the dynamical arrest diagram of Fig. 18, we have considered confocal microscopy data of colloidal HS binary mixtures. In addition to the samples reported above, we have also investigated samples with size ratio $\delta = 0.09$, $\phi \approx 0.60$, and different compositions x_s, as previously reported [32]. A series of transitions to arrested and ergodic states were observed for the big species in terms of their MSD (inset of Fig. 18). In the absence of

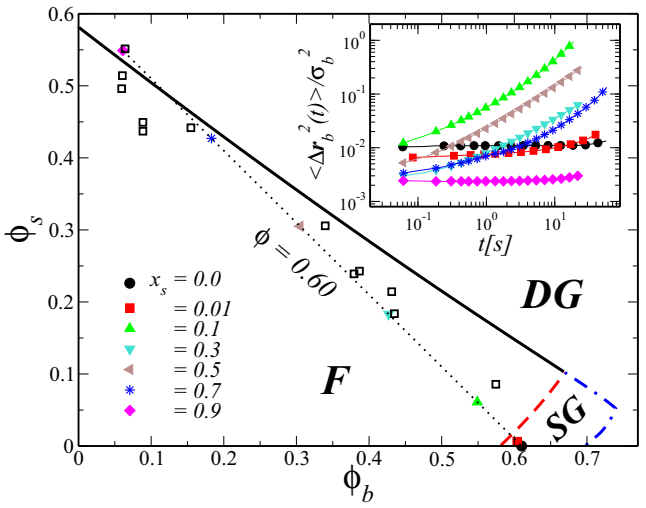

FIG. 18. State space defined by the volume fractions of big ϕ_b and small ϕ_s particles of a binary mixture of HS with size ratio $\delta = 0.1$. Lines are predictions for the glass transition provided by the SCGLE theory, determined using Eq. (C4) and the PY-VW approximation for the static structure matrix $\boldsymbol{S}(q)$. The solid line describes the transitions from the fluid (F) to the double-glass (DG) state. The dashed line indicates the transitions between the (F) and the single-glass (SG) states. The dashed-dotted line shows the transition from the SG to the double-glass DG state. The different state points represented by solid symbols along the dotted line correspond to those previously investigated by means of confocal microscopy experiments in Ref. [32]. The open squares instead describe the glassy samples reported in Ref. [30] Inset: measured MSD of the large spheres for different compositions x_s (as indicated), constant volume fraction $\phi \approx 0.60$, and size ratio $\delta = 0.09$ taken from Ref. [32].

small particles, $x_s = 0.0$ (solid circle), the one-component system of large spheres exhibits dynamical arrest, mainly characterized by a long-time *plateau* in the MSD, and with a characteristic localization length $l^*_b \equiv l_b/\sigma_b \sim 0.1$. For $x_s = 0.01$ (solid square), the big particles remain arrested and display a slightly smaller l^*_b. Consistently, the SCGLE predicts that both state points belong to region SG. At $x_s = 0.1$ (solid triangle), the MSD shows diffusive behavior indicating that the glassy state of the big spheres is *melted*. According to the theory, this state is now located inside the ergodic region F. Increasing the fraction of small particles to $x_s = 0.3$ (solid down triangle), the MSD slows down and appears subdiffusive, and for $x_s = 0.5$ (solid side triangle) an acceleration is observed. At $x_s = 0.7$ (asterisk), there is a further slowing down of the MSD. According to the theory, this state point approaches the transition line separating regions F and DG. Finally, for $x_s = 0.9$ (solid diamond), the dynamics of the large particles becomes arrested again, but with a smaller localization length ($l^*_b \approx 0.05$) in comparison to the cases $x_s = 0.0$ and 0.1, consistent with the presence of a glass of small spheres. According to the theory, this state point belongs to region DG, thus providing qualitative consistency between the SCGLE and these experimental results.

Despite this qualitative agreement, we should also refer to the experimental samples of Ref. [30], shown as the open

squares in Fig. 18 and reporting glassy samples for the case $\delta = 0.1$. The qualitative results are essentially the same: both show that, above a certain threshold for ϕ_s, the total volume fraction of the mixture to reach the glass transition becomes smaller with increasing ϕ_s (otherwise, a line adjusting the experimental data would be parallel to that describing the experiments of Ref. [32]). In this case, however, the quantitative agreement between theory and experiments is poor since the SCGLE overestimate the locus of the transition line. This difference may be attributed to several factors such as polydispersity, residual charges, and other effects present in the experimental samples but not in the theory, in particular, hydrodynamic interactions. Furthermore, one should also consider the simplified character of the theory which does neither account for these effects and uses the Percus-Yevick approximation combined with the Verlet-Weiss correction for the static structure factor.

3. Collective dynamics of the F-SG transition

The SG domain describes a region of partially arrested states, where the collective dynamics of both species is predicted to undergo dynamical arrest, whereas the self-dynamics of the small particles remains ergodic. This feature of the F-SG transition was observed through the decoupling of the SISF, $F_b^S(q^* = 7.18, t)$ and $F_s^S(q^* = 7.18)$ [Figs. 2(a) and 2(b)], and of the corresponding MSDs $\langle[\Delta \mathbf{r}_i(t)]^2\rangle$ (Fig. 7).

The collective dynamics, however, shows a subtle feature that deserves to be briefly commented. Collective diffusion is conventionally described in terms of the so-called *normalized* ISF, $f_{ii}(q,t) \equiv F_{ii}(q,t)/S_{ii}(q)$, defined in terms of the diagonal elements of the matrix $\boldsymbol{F}(q,t)$ of Eq. (C1) and the initial values $F_{ii}(q, t = 0) = S_{ii}(q)$, being the quantities accessible experimentally. These observables were extensively investigated in this work combining DDM experiments, MD simulations, and theoretical calculations. Toward the F-SG transition, both $f_{bb}(q^* = 7.18, t)$ and $f_{ss}(q^* = 7.18)$ display a slowing down in the relaxation and become strongly correlated [see, for instance, Figs. 2(c) and 2(d)]. This suggests that, at the level of collective dynamics, it is only possible to detect either fluid or arrested states, but not partially arrested ones. This, however, is only the result of the convention adopted to describe collective dynamics and, hence, of the *normalization* employed in the solution of Eq. (C1). To see this, let us consider the collective *propagator* matrix $\boldsymbol{\Psi}(q,t) \equiv \boldsymbol{F}(q,t)\boldsymbol{S}^{-1}(q)$, with initial condition $\boldsymbol{\Psi}(q, t = 0) = \boldsymbol{I}$. The quantity $\Psi_{\alpha\beta} \equiv [\boldsymbol{\Psi}]_{\alpha\beta}$ can be interpreted as the effect of the static structure associated to the species β on the collective dynamics of species α.

In terms of the diagonal *propagators* $\Psi_{bb}(q,t)$ and $\Psi_{ss}(q,t)$, the scenario for the collective dynamics of the F-SG transition differs from that displayed by the ISF $f_{bb}(q,t)$ and $f_{ss}(q,t)$. Specifically, one finds that the collective propagator $\Psi_{bb}(q^* = 7.18, t)$ displays dynamical arrest, whereas $\Psi_{ss}(q^* = 7.18, t)$ decays to zero, in qualitative analogy with the behavior of the self-ISFs (for a detailed discussion, the reader is referred to Sec. IV of Ref. [37]). These conditions are illustrated in Fig. 19 by the results for $\Psi_{bb}(q^* = 7.18, t)$ and $\Psi_{ss}(q^* = 7.18, t)$ calculated at the state point ($\delta = 0.2$, $\phi_b = 0.638$, $\phi_s = 0.05$), corresponding to the intersection of path *S1* with the F-SG transition line (see Fig. 1). In the same figure, the behavior of both f_{bb} and f_{ss} at the same state point is displayed for comparison.

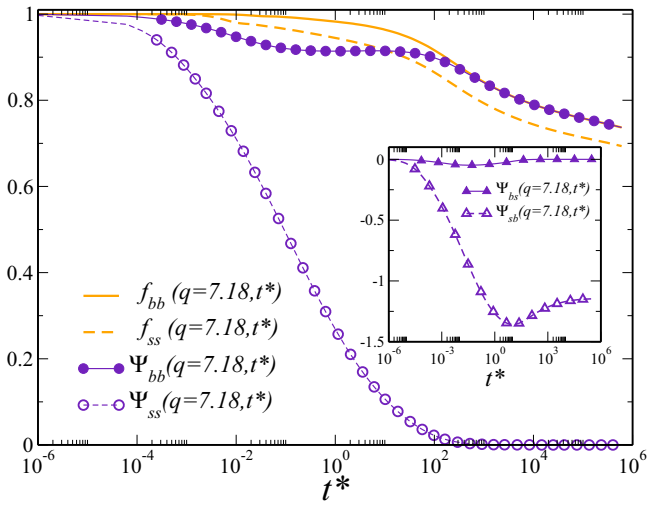

FIG. 19. Comparison of the behavior of the collective ISF $f_{bb}(q^* = 7.18, t^*)$ (solid line) and $f_{ss}(q^* = 7.18, t^*)$ (dashed line), and the collective propagators $\Psi_{bb}(q^* = 7.18, t^*)$ (solid circles) and $\Psi_{ss}(q^* = 7.18, t^*)$ (empty circles), calculated at the state point ($\delta = 0.2$, $\phi_b = 0.638$, $\phi_s = 0.05$), corresponding to the intersection of path *S1* with the SG transition line in Fig. 1. Inset shows the behavior of the *crossed* propagators $\Psi_{bb}(q* = 7.18, t^*)$ (solid triangles) and $\Psi_{ss}(q* = 7.18, t^*)$ (empty triangles) at the same state point.

The relaxation of the *crossed* propagators $\Psi_{bs}(q,t)$ and $\Psi_{sb}(q,t)$ also deserves a comment, in particular, in connection with partially arrested states. First, one must have in mind that, despite the matrices $\boldsymbol{F}(q,t)$ and $\boldsymbol{S}(q)$ being symmetric, the product $\boldsymbol{F}(q,t)\boldsymbol{S}^{-1}(q)$, in general, is not, in other words $\Psi_{bs}(q,t) \neq \Psi_{sb}(q,t)$. Second, since $\boldsymbol{\Psi}(q, t = 0) = \boldsymbol{I}$, it is clear that $\Psi_{bs}(q, t = 0)$ and $\Psi_{sb}(q, t = 0)$ must vanish. Third, the off-diagonal elements of $\boldsymbol{\Psi}(q,t)$ are not necessarily positive. In the inset of Fig. 19, the behavior of these propagators at the aforementioned state point in the F-SG transition line is shown. One observes that both quantities are negative and that Ψ_{sb} relaxes to a finite nonergodic asymptotic value, although Ψ_{bs} is always much smaller and relaxes to zero. On the other hand, it is straightforward to show that $f_{bb}(q,t) = \Psi_{bb}(q,t) + [S_{sb}(q)/S_{bb}(q)]\Psi_{bs}(q,t)$ and $f_{ss}(q,t) = \Psi_{ss}(k,t) + [S_{bs}(q)/S_{ss}(q)]\Psi_{sb}(q,t)$. Hence, since $\Psi_{bs}(q,t)$ is small and relaxes to zero, one finds that both f_{bb} and Ψ_{bb} display similar behavior. In contrast, although the propagator Ψ_{ss} does decay to zero, f_{ss} exhibits dynamic arrest due to its linear dependence on $\Psi_{sb}(q,t)$, which, as illustrated in the inset of Fig. 19, relaxes to a nonzero value.

Thus, at the F-SG transition, only the $\Psi_{\alpha\beta}(q,t)$ associated with $\beta = b$ do not relax to zero, which indicates that in the single glass, the big particles' static structure affects the glassy (long-time) dynamics of the small species, but the glassy dynamics of large spheres is not influenced by the static structure of the small particles (but only by their dynamics).

[1] A. L. Greer, Metallic glasses, Science **267**, 1947 (1995).

[2] A. Meyer, Atomic transport in dense multicomponent metallic liquids, Phys. Rev. B **66**, 134205 (2002).

[3] Th. Voigtmann, A. Meyer, D. Holland-Moritz, S. Stüber, T. Hansen, and T. Unruh, Atomic diffusion mechanisms in a binary metallic melt, Europhys. Lett. **82**, 66001 (2008).

[4] K. Zhang, W. W. Smith, M. Wang, Y. Liu. J. Schroers, M. D. Shattuck, and C. S. O'Hern, Connection between the packing efficiency of binary hard spheres and the glass-forming ability of bulk metallic glasses, Phys. Rev. E **90**, 032311 (2014).

[5] I. M. Hodge, Physical aging in polymer glasses, Science **267**, 1945 (1995).

[6] C. A. Angell, Formation of glasses from liquids and biopolymers, Science **267**, 1924 (1995).

[7] L. Cipelletti and L. Ramos, Slow dynamics in glassy soft matter, J. Phys.: Condens. Matter **17**, R253 (2005).

[8] P. N. Segré, V. Prasad, A. B. Schofield, and D. A. Weitz, Glasslike Kinetic Arrest at the Colloidal-Gelation Transition, Phys. Rev. Lett. **86**, 6042 (2001).

[9] S. Zahid, A. T. Shah, A. Jamal, A. A. Chaudhry, A. S. Khan, A. F. Khan, N. Muhammad, and Ihtesham ur Rehman, Biological behavior of bioactive glasses and their composites, RSC Adv. **6**, 70197 (2016).

[10] W. van Megen and P. N. Pusey, Dynamic light-scattering study of the glass transition in a colloidal suspension, Phys. Rev. A **43**, 5429 (1991).

[11] W. van Megen and S. M. Underwood, Glass Transition in Colloidal Hard Spheres: Mode-Coupling Theory Analysis, Phys. Rev. Lett. **70**, 2766 (1993).

[12] F. Sciortino and P. Tartaglia, Glassy colloidal systems, Adv. Phys. **54**, 471 (2005).

[13] G. L. Hunter and E. R. Weeks, The physics of the colloidal glass transition, Rep. Prog. Phys. **75**, 066501 (2012).

[14] P. J. Lu, E. Zacarelli, F. Ciulla, A. B. Schofield, F. Sciortino, and D. A. Weitz, Gelation of particles with short-range attraction, Nature (London) **453**, 499 (2008).

[15] E. Zacarelli and W. C. K. Poon, Colloidal glasses and gels: The interplay of bonding and caging, Proc. Natl. Acad. Sci. USA **106**, 15203 (2009).

[16] A. P. R. Eberle, N. J. Wagner, and R. Castañeda-Priego, Dynamical Arrest Transition in Nanoparticle Dispersions with Short-Range Interactions, Phys. Rev. Lett. **106**, 105704 (2011).

[17] K. N. Pham, A. M. Puertas, J. Bergenholtz, S. U. Egelhaaf, A. Moussaïd, P. N. Pusey, A. B. Schofield, M. E. Cates, M. Fuchs, and W. C. K. Poon, Multiple glassy states in a simple model system, Science **296**, 104 (2002).

[18] K. N. Pham, S. U. Egelhaaf, P. N. Pusey, and W. C. K. Poon, Glasses in hard spheres with short-range attraction, Phys. Rev. E **69**, 011503 (2004).

[19] T. Eckert and E. Bartsch, Re-entrant Glass Transition in a Colloid-Polymer Mixture with Depletion Attractions, Phys. Rev. Lett. **89**, 125701 (2002).

[20] S. Vivek, C. P. Kelleher, P. M. Chaikin, and E. R. Weeks, Long-wavelength fluctuations and the glass transition in two dimensions and three dimensions, Proc. Natl. Acad. Sci. USA **114**, 1850 (2017).

[21] D. Heckendorf, K. J. Mutch, S. U. Egelhaaf, and M. Laurati, Size-Dependent Localization in Polydisperse Colloidal Glasses, Phys. Rev. Lett. **119**, 048003 (2017).

[22] K. A. Dawson, The glass paradigm for colloidal glasses, gels, and other arrested states driven by attractive interactions, Curr. Opin. Colloid Interf. Sci. **7**, 218 (2002).

[23] C. Mayer, F. Sciortino, C. N. Likos, P. Tartaglia, H. Löwen, and E. Zacarelli, Multiple glass transitions in star polymer mixtures: Insights from theory and simulations, Macromolecules **42**, 423 (2009).

[24] N. Khali, A. de Candia, A. Fierro, M. Pica Ciamarra, and A. Coniglio, Dynamical arrest: Interplay of glass and gel transitions, Soft Matter **10**, 4800 (2014).

[25] E. R. Weeks and D. A. Weitz, Properties of Cage Rearrangements Observed near the Colloidal Glass Transition, Phys. Rev. Lett. **89**, 095704 (2002).

[26] S. R. Williams and W. van Megen, Motions in binary mixtures of hard colloidal spheres: Melting of the glass, Phys. Rev. E **64**, 041502 (2001)

[27] J. M. Lynch, G. C. Cianci, and E. R. Weeks, Dynamics and structure of an aging binary colloidal glass, Phys. Rev. E **78**, 031410 (2008).

[28] T. Narumi, S. V. Franklin, K. W. Desmond, M. Tokuyama, and E. R. Weeks, Spatial and temporal dynamical heterogeneities approaching the binary colloidal glass transition, Soft Matter **7**, 1472 (2011).

[29] A. Imhof and J. K. G. Dhont, Long-time self-diffusion in binary colloidal hard-sphere dispersions, Phys. Rev. E **52**, 6344 (1995).

[30] A. Imhof and J. K. G. Dhont, Experimental Phase Diagram of a Binary Colloidal Hard-Sphere Mixture with a Large Size Ratio, Phys. Rev. Lett. **75**, 1662 (1995).

[31] T. Sentjabrskaja, M. Hermes, W. C. K. Poon, C. D. Estrada, R. Castañeda-Priego, S. U. Egelhaaf, and M. Laurati, Transient dynamics during stress overshoots in binary colloidal glasses, Soft Matter **10**, 6546 (2014).

[32] J. Hendricks, R. Capellmann, A. B. Schofield, S. U. Egelhaaf, and M. Laurati, Different mechanisms for dynamical arrest in largely asymmetric binary mixtures, Phys. Rev. E **91**, 032308 (2015).

[33] T. Sentjabrskaja, E. Zaccarelli, C. De Michele, F. Sciortino, P. Tartaglia, Th. Voigtmann, S. U. Egelhaaf, and M. Laurati, Anomalous dynamics of intruders in a crowded environment of mobile obstacles, Nat. Commun. **7**, 11133 (2016).

[34] M. Laurati, T. Sentjabrskaja, J. Ruiz-Franco, S. U. Egelhaaf, and E. Zaccarelli, Different scenarios of dynamic coupling in glassy colloidal mixtures, Phys. Chem. Phys. Chem. **20**, 18630 (2018).

[35] Th. Voigtmann and W. Götze, Effect of composition changes on the structural relaxation of a binary mixture, Phys. Rev. E **67**, 021502 (2003).

[36] Th. Voigtmann, Multiple glasses in asymmetric binary hard spheres, Europhys. Lett. **96**, 36006 (2011).

[37] R. Juárez-Maldonado and M. Medina-Noyola, Theory of dynamic arrest in colloidal mixtures, Phys. Rev. E **77**, 051503 (2008).

[38] R. Juárez-Maldonado and M. Medina-Noyola, Alternative View of Dynamic Arrest in Colloid-Polymer Mixtures, Phys. Rev. Lett. **101**, 267801 (2008).

[39] A. J. Moreno and J. Colmenero, Relaxation scenarios in a mixture of large and small spheres: Dependence on the size disparity, J. Chem. Phys. **125**, 164507 (2006).

[40] Th. Voigtmann and J. Horbach, Double Transition Scenario for Anomalous Diffusion in Glass-Forming Mixtures, Phys. Rev. Lett. **103**, 205901 (2009).
[41] W. Götze, in *Liquids, Freezing and Glass Transition*, edited by J. P. Hansen, D. Levesque, and J. Zinn-Justin (North-Holland, Amsterdam, 1991).
[42] W. Götze and L. Sjögren, Relaxation processes in supercooled liquids, Rep. Prog. Phys. **55**, 241 (1992).
[43] W. Götze, The essentials of the mode-coupling theory for glassy dynamics, Condens. Matter Phys. **1**, 873 (1998).
[44] W. Götze, *Complex Dynamics of Glass-Forming Liquids. A Mode-Coupling Theory* (Oxford University Press, Oxford, 2009).
[45] L. Yeomans-Reyna and M. Medina-Noyola, Self-consistent generalized Langevin equation for colloid dynamics, Phys. Rev. E **64**, 066114 (2001).
[46] L. Yeomans-Reyna, M. A. Chávez-Rojo, P. E. Ramírez-González, R. Juárez-Maldonado, M. Chávez Páez, and M. Medina-Noyola, Dynamic arrest within the self-consistent generalized Langevin equation of colloid dynamics, Phys. Rev. E **76**, 041504 (2007).
[47] M. A. Chávez-Rojo and M. Medina-Noyola, Self-consistent generalized Langevin equation for colloidal mixtures, Phys. Rev. E **72**, 031107 (2005); **76**, 039902(E) (2007).
[48] R. Juárez-Maldonado, M. A. Chávez-Rojo, P. E. Ramírez-González, L. Yeomans-Reyna, and M. Medina-Noyola, Simplified self-consistent theory of colloid dynamics, Phys. Rev. E **76**, 062502 (2007).
[49] L. F. Elizondo-Aguilera and Th. Voigtmann (unpublished).
[50] J. K. Percus and G. J. Yevick, Analysis of classical statistical mechanics by means of collective coordinates, Phys. Rev. **110**, 1 (1958).
[51] L. Verlet and J.-J. Weis, Equilibrium theory of simple liquids, Phys. Rev. A **5**, 939 (1972).
[52] E. Lázaro-Lázaro, P. Mendoza-Méndez, L. F. Elizondo-Aguilera, J. A. Perera-Burgos, P. E. Ramírez-González, G. Pérez-Ángel, R. Castañeda-Priego, and M. Medina-Noyola, Self-consistent generalized Langevin equation theory of the dynamics of multicomponent atomic liquids, J. Chem. Phys. **146**, 184506 (2017).
[53] L. F. Elizondo-Aguilera and M. Medina-Noyola, Localization and dynamical arrest of colloidal fluids in a disordered matrix of polydisperse obstacles, J. Chem. Phys. **142**, 224901 (2015).
[54] W. C. K. Poon, E. R. Weeks, and C.-P. Royall, On measuring colloidal volume fractions, Soft Matter **8**, 21 (2012).
[55] M. Medina-Noyola and P. Ramírez-González, Non-equilibrium relaxation and near-arrest dynamics in colloidal suspensions, J. Phys.: Condens. Matter **21**, 504103 (2009).
[56] P. E. Ramírez-González and M. Medina-Noyola, General nonequilibrium theory of colloid dynamics, Phys. Rev. E **82**, 061503 (2010); Aging of a homogeneously quenched colloidal glass-forming liquid, *ibid.* **82**, 061504 (2010).
[57] L. E. Sánchez-Díaz, E. Lázaro-Lázaro, J. M. Olais-Govea, and M. Medina-Noyola, Non-equilibrium dynamics of glass-forming liquid mixtures, J. Chem Phys. **140**, 234501 (2014).
[58] P. Mendoza-Méndez, E. Lázaro-Lázaro, L. E. Sánchez-Díaz, P. E. Ramírez-González, G. Pérez-Ángel, and M. Medina-Noyola, Crossover from equilibration to aging: Nonequilibrium theory versus simulations, Phys. Rev. E **96**, 022608 (2017).
[59] M. C. Vargas and G. Pérez-Ángel, Crystallization time scales for polydisperse hard-sphere fluids, Phys. Rev. E **87**, 042313 (2013).
[60] L. López-Flores, P. Mendoza-Méndez, L. E. Sánchez-Díaz, L. L. Yeomans-Reyna, A. Vizcarra-Rendón, G. Pérez-Ángel, M. Chávez-Páez, and Magdaleno Medina-Noyola, Dynamic equivalence between atomic and colloidal liquids, Europhys. Lett. **99**, 46001 (2012).
[61] L. López-Flores, L. L. Yeomans-Reyna, M. Chávez-Páez, and Magdaleno Medina-Noyola, The overdamped van Hove function of atomic liquids, J. Phys.: Condens. Matter **24**, 375107 (2012).
[62] L. López-Flores, H. Ruiz Estrada, M. Chávez-Páez, and M. Medina-Noyola, Dynamic equivalences in the hard-sphere dynamic universality class, Phys. Rev. E **88**, 042301 (2013).
[63] P. Mendoza-Méndez, L. López-Flores, A. Vizcarra-Rendón, L. E. Sánchez-Díaz, and M. Medina-Noyola, Generalized Langevin equation for tracer diffusion in atomic liquids, Phys. A (Amsterdam) **394**, 1 (2014).
[64] A. Yethiraj and A. van Blaaderen, A colloidal model system with an interaction tunable from hard sphere to soft and dipolar, Nature (London) **421**, 513 (2003).
[65] C. P. Royall, W. C. K. Poon, and E. Weeks, In search of colloidal hard spheres, Soft Matter **9**, 17 (2013).
[66] W. Schaertl and H. Sillescu, Brownian dynamics of polydisperse colloidal hard spheres: Equilibrium structures and random close packings, J. Stat. Phys. **77**, 1007 (1994).
[67] K. W. Desmond and E. R. Weeks, Influence of particle size distribution on random close packing of spheres, Phys. Rev. E **90**, 022204 (2014).
[68] T. G. Mason, Estimating the viscoelastic moduli of complex fluids using the generalized Stokes-Einstein equation, Rheol. Acta **39**, 371 (2000).